M. Phil.

RADIATION INDUCED STRUCTURAL MAGNETIC AND ELECTRIC TRANSFORMATIONS IN Al SUBSTITUTED Ni-Cu-Cd NANOPARTICLES

RADIATION INDUCED STRUCTURAL MAGNETIC AND ELECTRIC TRANSFORMATIONS IN Al SUBSTITUTED Ni-Cu-Cd NANOPARTICLES

By

BISHAKAR SHARMA

MASTER of PHILOSOPHY in PHYSICS

Student ID: 14MPHY012P

[Dept. of PHYSICS]

[2023]

DEPARTMENT OF PHYSICS

Chittagong University of Engineering & Technology, Chattogram-4349,

Bangladesh.

December - 2023

RADIATION INDUCED STRUCTURAL MAGNETIC AND ELECTRIC TRANSFORMATIONS IN Al SUBSTITUTED Ni-Cu-Cd NANOPARTICLES

By

BISHAKAR SHARMA

MASTER of PHILOSOPHY in PHYSICS

Student ID: 14MPHY012P

A thesis submited in partial fulfilment of the requierments for the degree of MASTER of PHILOSOPHY

DEPARTMENT OF PHYSICS

CHITTAGONG UNIVERSITY OF ENGINEERING & TECHNOLOGY

CHITTAGONG 4200, BANGLADESH

2023

DECLARATION

I hereby declare that the work contained in this Thesis has not been previously submitted to meet the requirements for an award at this or any other higher education institution. To the best of my knowledge and belief, the Thesis contains no materials previously published or another person except where due reference is cited. Furthermore, the Thesis complies with the PLAGIARISM and ACADEMIC INTEGRITY regulations of CUET.

.

BISHAKAR SHARMA

Student ID: 14MPHY012P

Department of Physics

Chittagong University of Engineering and Technology (CUET)

DEDICATED TO
MY PARENTS

List of Publication

Journal Article

- Bishakar Sharma and M. Belal Hossen*, “Radiation-induced structural and electric properties of Al-substituted NiCuCd nanoparticles”, J Mater Sci: Mater Electron (2022), 33:19036–19056, August 2022. 10.1007/s10854-022-08742-4.

Conference

- Bishakar Sharma and M. Belal Hossen*, “Effects of Gamma Irradiations on the Structural and Electrical Transport Properties of NiCuCd Ferrites Nanoparticles”, 2nd International Conference on Physics for Sustainable Development and Technology (ICPSDT-2017), CUET, 10-11 December, 2017.
- M. Bishakar Sharma , M. Amirul Islam and M. Belal Hossen, “Effects of Gamma Irradiation on the Structural, Magnetic and Electric Properties of NiCuCd Nanoparticles”, International Conference on Physics for sustainable Development, 08-10 March, 2018.

Declaration of Supervisor

This is to certify that Bishakar Sharma, Student ID 14MPHY012P has carried out this research work under my supervision and, he has fulfilled the relevant Academic Ordinance of Chittagong University of Engineering and Technology so that he is qualified to submit the following Thesis in the application for the degree of MASTER of PHILOSOPHY in Physics. Furthermore, the Thesis complies with the PLAGIARISM and ACADEMIC INTEGRITY regulations of CUET.

Dr. Mohammad Belal Hossen

Professor

Department of Physics

Chittagong University of Engineering and Technology (CUET)

Acknowledgment

All praises is due to God for whom I am here in the World to do this type of research works and I pray Him to accept this as the good deed.

I am extremely delighted to express my deepest sense of gratitude and honor to my supervisor Prof. Dr. Mohammad Belal Hossen, Department of Physics, Chittagong University of Engineering and Technology (CUET), Chattogram-4349, Bangladesh. He is enthusiastic Physicists, from whom I had the privilege of learning not only research work but also basic knowledge of Physics. His unbelievable motivation and guidance helped me to continue and complete my thesis work. I would like to thank the rest of the members of my examination committee for their encouragement and valuable comments.

I am sincerely greatful to Prof. Swapan Kumar Roy, Head, Department of Physics, (CUET), for his inspiration during the research work.

I would also like to express my gratitude to all other faculty members in the Department of Physics, CUET to suggest and help me positively.

I am grateful to Mr. Sohel Rana, Technical officer, CUET postgraduate Lab for co-operation at the time of sample synthesis and other technical supports. Thanks also to other officers and staff of the Department of Physics.

I also Would Like to express my deep gratitude to M. Faishal Mahmood, Ph.D. research fellow, M. Shahbaz Khan, M.Sc. research fellow and Prof. Al Amin M. Sirajul Islam, Head, Physics Department, Chittagong College for his continuous help and friendship during his work.

I would like to thank the Governing Body and colleagues of Shaheed N.M.M.J Degree College, Bakalia, Chattogram for giving permission to complete the degree.

Last but not the least I would like to give my special thanks to my parents, and my beloved wife Rani Das, because of their continuous unconditional supports along with patience towards the completion of this research work. Specially without having mental supports from my wife this degree might not be possible.

The Author

December, 2023 (Bishakar Sharma)

Abstract

The effect of gamma (γ) irradiations on the physical, magnetic and electrical properties of nanoferrites samples with a chemical formula of $Ni_{0.5}Cu_{0.2}Cd_{0.3}Fe_{2-x}Al_xO_4$ have studied. These samples have prepared by sol-gel auto combustion method. The synthesized samples have irradiated for γ rays from ^{60}Co source at room temperature with a dose of 1 and 3 MRad, at a dose rate of 1.067 MRad/h. X-ray diffraction (XRD) parameters, magnetization, dielectric constant, dielectric loss factor, electric modulus, impedance and ac conductivity have analyzed for the irradiated samples. XRD patterns show that the irradiation has caused a change in the lattice constant due to ions redistribution. The lattice constant of the investigated samples has increased with the increase in irradiation (gamma) due to the conversion of Fe^{3+} (0.67Å) to Fe^{2+} (0.76Å). Moreover, the cation redistribution play an important role in increasing the values of ac conductivity with increasing the irradiation (gamma) dose.

The magnetization has measured by using Vibrating Sample Magnetometer at room temperature with an applied field of 1.5 T (in $\mu_0 H$) after irradiation (gamma) by different doses. The saturation magnetization initially increase with irradiation. The frequency dependence of conductivity, dielectric constant, and dielectric loss has been studied. The Cole-Cole plots of ($Z^{//}$ vs $Z^{/}$) give different two over lapping incomplete semicircles depending upon the electrical parameters. Also, the modulus plots of ($M^{//}$ vs $M^{/}$) insure that the electric stiffness is the dominant property of the investigated samples. Electrical and dielectric properties have carried out with the influence of γ irradiation and interpret using existing theories.

বিমূর্ত

$Ni_{0.3}Cu_{0.2}Cd_{0.3}Fe_{2-x}Al_xO_4$ এর ন্যানো কণা sol-gel পদ্ধতিতে প্রস্তুত করা হয়েছে। তারপর প্রয়োজনীয় পরিমাণ নমুনাগুলিকে কক্ষ তাপমাত্রায় $^{64}Co_{৭}$ গামাডোজ উৎস হতে নিঃসৃত 1 MRad এবং 3 MRad গামাডোজ দিয়ে বিকিরিত করা হয়েছিল। ^{64}Co গামা উৎস থেকে প্রতি ঘন্টায় 1.067 MRad ডোজ γ-রশ্মি বিকিরণে বিকিরিত করার ফলে $Ni_{0.3}Cu_{0.2}Cd_{0.3}Fe_{2-x}Al_xO_4$ এর গাঠনিক, বৈদ্যুতিক, পরাবৈদ্যুতিক ও চুম্বকীয় ধর্মের পরিবর্তন অনুসন্ধান করাই এই গবেষণার লক্ষ্য। XRD এর ফলাফল গুলি বিকিরণের প্রভাব প্রধানত ফেরিক (Fe^{3+}) থেকে ফেরাস (Fe^{2+}) রূপান্তরের জন্য lattice ধ্রুবকের মান বৃদ্ধি পেয়েছে। গবেষণার ফলাফল বিশ্লেষনে দেখা যায় যে, বিকিরণের ডোজ বৃদ্ধির সাথে সাথে প্রতিটি নমুনার AC পরিবাহিকতার মান বাড়তে থাকে এবং ধনাত্মক আয়নের এর পূর্ণবন্টনে ভূমিকা পালন করে কম্পাঙ্ক নির্ভর ডাই ইলেকট্রিক ধ্রুবক পরিবাহিতা এবং ডাই ইলেকট্রিক loss tangent বিকিরণের মান পরিবর্তনে ভূমিকা পালন করে। Cole-Cole plot দুটি উপরিপাতন অসম্পূর্ণ অর্ধবৃত্তকে চিহ্নিত করে যা সমতল (RC) সার্কিট দ্বারা ফিট করে উপাত্ত পাওয়ার জন্য বিশ্লেষণ করা হয়। পরীক্ষামূলক এবং তাত্ত্বিক বিশ্লেষণ সেই সাথে বিকিরণের পরে প্রভাবশালী Fe^{+2} গঠনের কারণে grain-grain boundary রোধের উল্লেখযোগ্য হ্রাস লক্ষ করা গেছে। এই বিশ্লেষণ গুলিতে বিশেষ অগ্রাধিকার তেজস্ক্রিয় ক্ষেত্রে প্রয়োগ রয়েছে (উদাহরণস্বরূপ পারমানিক চুল্লি ব্যবহার সুবিধা) কারণ চুম্বক উপাদান গুলির জন্য এগুলিতে ফেরাইটে কর্মদক্ষতা মূল্যায়ন করা হয়েছে। কক্ষ তাপমাত্রায় 1.5 (μ_oH) টেসলা প্রয়োগ চুম্বকক্ষেত্রসহ একটি নমুনা চুম্বকায়ন বাস্তবায়নের মাধ্যমে, গামা (γ) বিকিরণের পরে চুম্বকীয়তা পরিমান করা হয়। VSM পরীক্ষায় দেখা যায় যে, বিকিরণের পরে সম্পৃক্ত চুম্বকীয়তা (M_s) বৃদ্ধি পেয়েছে। অন্যদিকে বিকিরণ করা ন্যানো ফেরাইটের চৌম্বকীয় আচরণটি Law of Approach to Saturation (LAS) এর বিশ্লেষণ দ্বারা আলোচনা করা হয়েছে।

TABLE OF CONTENTS

LIST OF FIGURES

LIST OF TABLES

NOMENCLATURE

Symbol	Details
MRI	Magnetic resonance imaging
XRD	X-ray diffraction
M_s	Saturation magnetization
VSM	Vibrating Sample Magnetometer
Gy	Gray
MeV	Mega electron Volt
hkl	Miller index
μ_{PE}	Photoelectric attenuation coefficient
n,p	Neutron-proton
MRad	Mega Rad
SHI	Swift heavy ion
$tan\delta$	Dielectric loss tangent
σ_{ac}	ac conductivity
ρ_X	X-ray density
N-R	Nelson Riley function
M'	Real part of electric modulus
M''	Imaginary part of electric modulus
ε'	Real part of complex permittivity
ε''	Imaginary part of complex permittivity
Z'	Real part of complex impedance
Z''	Imaginary part of complex impedance

CHAPTER 1: INTRODUCTION

1.1 BACKGROUND

The process of creating new materials with particular characteristics in the nanometric range and their applications is often reffered as nanotechnology. As a consequence nanotechnology also involves the low-cost manufacturing of nanoscale devices with special uses [1]. Synthesis and accurate characterization of nanoparticles play a crucial role in present nanotechnology era. It is thought that nanoparticles serve as a link between atomic as well as molecule and bulk structures. These characteristics make these materials extremely interesting for both scientific research and technological development [2]. Aside from the improved physical characteristics of nanocrystalline materials, it is critical to advance scientific research more quickly in a number of areas [3]. Applications in electronics and telecommunications have made use of high resistivity and high-frequency effectiveness [4]. The process used to synthesize nano ferrites has an impact on not only particle size but also electrical transport and magnetic characteristics [5-7]. Many studies on the effects of γ-irradiation on compounds have been conducted in the past few decades. For example, gamma ions with high energy for ferrite structure might cause dramatic structural and magnetic changes in nano form samples of garnets, hexa-ferrites, spinel, and other materials. Tetrahedral (A) and octahedral (B) sites combined with metal ion engravings make up the spinel structures. There is a fcc oxygen cage around these ions. The anti-ferrimagnetic magnetic transitions between metallic ions are dependent on the places where the magnetic ions are occupied as well as their placement in crystallography. Thus, the chosen issue is the rearrangement of cations on the spinel ferrites or the displacement of cations for due directional and bonding length alterations.

In addition to studying magnetic characteristics, more research is being done on electrical and dielectric properties from a basic and applied standpoint. The preparation process, along with environment, the heat treatment temperature, and the proportion of existing chemicals etc. affect the dielectric characteristics. Thus, when this substance is exposed to radiation through the use of radiant energy, new kinds of occurrences have emerged, which can alter dielectric and magnetic properties drastically for technical applications.

Numerous studies have documented the remarkable characteristics of ferromagnetic oxides when exposed to high and low energy ions, electrons, c-photons, and fast neutrons. The effects of exposure to ^{60}Co radioactive source γ-rays at dosages of 1 MRad and 2 MRad on the structural, magnetic, and electrical characteristics of Mg-Cu-Zn and Ni-Cu-Zn nano ferrites were studied by Assar et al [8]. According to the XRD data, when the irradiation dosage is increased for Ni–Cu–Zn ferrite samples, the disordered grain border area increases at the cost of the ordered regions of the crystallites, or grains. This causes the crystallite size to decrease. Also, the slight increase of the lattice constant of all investigated samples may be attributed to the conversion of some Fe^{3+} (0.67 Å) to Fe^{2+} (0.76 Å). The cation redistribution, which is primarily responsible for modifying the magnetic characteristics of the samples, is responsible for the observed increase in saturation and residual magnetization after irradiation. The samples' Cole–Cole ($Z^{//}$ vs. $Z^{/}$) plots reveal two partially overlapped semicircles and a notable shift in values with respect to radiation dosage. Ultimately, it is determined that both compositions exhibit balanced behavior with increasing exposure to γ-ray radiation, making them viable candidates for use in the production of MLCIs when subjected to extremely high irradiation levels. In a different study, Ahmed et al. [7] investigated the impact of laser and

gamma radiation on the physical characteristics of $MnFe_2O_4$, which was made using the citrate precursor approach.

Magnetic resonance scanners, computerized tomography, satellites, and nuclear fusion reactors are among the successful uses of gamma irradiation systems [9]. Irradiating ferrites with gamma rays is a useful technique for understanding controlled flaws that are formed in the form of points, columns, and clusters [10].

Since Cu-based ferrites have low processing temperatures and a simple synthesis procedure, they are the preferred magnetic material for MLCI. They also have appropriate electromagnetic characteristics for high-frequency applications [8]. Because of their adaptable soft magnetic properties, Ni–Cu–Cd nano ferrites might be used in high-frequency applications as an alternate of Ni-Cu-Zn ferrites. Because of their high resistivity, high magnetization, and chemical stability, these ferrites may thus be used in the MHz to GHz range [11]. A statistical redistribution (cations) governs the variations in the spinel structure's characteristics. Cations move more quickly from A-site to other B-site and vice-versa. It has observed that the impact of unirradiated and γ-irradiated zinc ferrites on electrical conduction [12]. This report also includes the same study on $CdFe_2O_4$, $Co_xZn_{1-x}Fe_2O_4$, and Fe_3O_4. Due to irradiation effects, issues have recently surfaced with the construction of electrical components for measurement devices and accelerators. Instead of a large dosage, cosmic radiation has been detected in the case of spacecraft and satellites.

Radiation might show signs of atom ionization, excitation, and matter structural disruption [13]. Of all radiations, c rays cause flaws in materials by altering their morphological, structural, and electromagnetic characteristics. These changes might be caused by cation inversion,

ferrimagnetic ordering breakdown, surface state pinning, etc. More elementary particles and radioactive isotopes are forced by recent advancements in nuclear engineering than by ionization radiation from different acts [14,15]. High-energy electromagnetic radiations have interacted with electronic shells when substances have been exposed to radiation. The scattering of both elastic and inelastic kinds that occur during atom ionization and excitation have given origin to the phrase radiation damage. In addition, this disturbance in the matter and nuclear initiations are another reason for that [16,17]. Gamma irradiation is now the subject of most research and development for medical equipment and cutting-edge industrial products, such as nuclear fusion reactors, computerized tomography spacecraft, magnetic resonance imaging, and satellites.

There are no works that have been reported regarding different irradiation effects comparison in the case of nano ferrite properties till now. The effective behaviors of $Ni_{0.5}Cu_{0.2}Cd_{0.3}Fe_{2-x}Al_xO_4$ were analyzed in a previous study [18] in which some noticeable results were obtained in synthesis, homogeneity in structure and morphology, resistivity, and magnetization with size in the nanoscale range. This is what draw interest in studying the behavior of the magnetic, structural, and electric characteristics when Ni–Cu–Cd–Al nano ferrites have exposed to gamma radiation. The objective is to observe the structural strength as well as electric and dielectric properties in addition to the preceding one for the $Ni_{0.5}Cu_{0.2}Cd_{0.3}Fe_{2-x}Al_xO_4$. The goal was to irradiate samples as an inexpensive method to produce distinct properties. This innovative approach yields a productive comparison of two primary irradiations, designated γ, as affected by electromagnetic waves and particles.

No research work has reported until now on the comparison of different irradiations on the structural, magnetic and electric properties of nano ferrites. For these reasons and for the first

time much attention has been paid in the present work to study the effect of gamma and neutron irradiation on the structural, magnetic, dielectric and electric properties of Ni-Cu-Cd-Al nanoparticles under investigation. Another goal is the variation of the physical properties of such nano ferrites ($Ni_{0.5}Cu_{0.2}Cd_{0.3}Fe_{2-x}Al_xO_4$) by using irradiation as a sample low cost tool to obtain novel characteristics. The novelty of this fruitful work is emphasized from the nature of the influence of γ-irradiation on nanoparticle.

1.2 AIMS AND OBJECTIVES

The main motive of current works are derived below:

i. Synthesis of $Ni_{0.5}Cu_{0.2}Cd_{0.3}Fe_{2-x}Al_xO_4$ (x = 0.00, 0.015, 0.03, 0.045, 0.06) nanoparticles.
ii. X-ray diffraction (XRD) patterns of the prepared nanoparticles after irradiation are recorded by X-ray diffract meter.
iii. The variation of saturation magnetization (M_s) for various irradiated composition are observed using Vibrating Sample Magnetometer.
iv. Frequency dependent transport properties such as complex dielectric constant, AC conductivity and analysis of complex impedance spectra (Cole-Cole plot) of different irradiated compositions are investigated.

1.3 THESIS OUTLINE

Outline has been organized in the following way:

Chapter 1: presents a brief introduction about "RADIATION INDUCED STRUCTURAL MAGNETIC AND ELECTRIC PROPERTIES OF Al SUBSTITUTED Ni-Cu-Cd NANOPARTICLES"; brief of previous work and organization of thesis.

Chapter 2: deals with detailed theoretical background to study this type of research work. Classified and described the magnetization term along with class of different materials. Detail in this chapter incorporates background information to assist in understanding the aims and objectives of this investigation, and also reviews recent reports by other investigators with which these results could be compared.

Chapter 3: incorporates with the detail of sample synthesis and experimental technique.

Chapter 4: describes the results and discussion of all studies.

Chapter 5: includes the general conclusions as well as key findings drawn from the overall experimental results and discussion along with the scopes of future work.

A concise list of publications and conferences related to present research work has been presented at the end.

CHAPTER 2: LITERATURE REVIEW

2.1 GENERAL

This section represents the comprehensive overview of the research, which includes the main topic of the thesis that will be covered in literature review. Here, key studies related to this research will be discussed along with their methods, findings and contributions to this regarding field.

2.2 RELATED THEORIES AND UNITS OF RADIATION MEASUREMENT

2.2.1 Exposure

When all of the electrons released by photons in a medium-volume element with mass Δm are fully stopped in the volume, the unit of exposure, X, is defined as the quotient of ΔQ divided by Δm. ΔQ is the total of electrical charges on all the ions of one sign that are produced in the medium,

$$X = \frac{\Delta Q}{\Delta m}$$

Roentgen (R) is the specific unit of exposure that comes before the SI system. Exposure does not have a SI unit, and the old special unit, roentgen, is no longer in use, but it is still infrequently encountered, especially in the older literature.

2.2.2 Absorbed Dose

The definition of the term "absorbed dose" D, is the product of Δm and ΔE_D, where Δm is the mass of matter in a volume element and ΔE_D is the energy deposited (E_D is equivalent to energy imparted, vide infra) by ionizing radiation:

$$D = \frac{\Delta E_D}{\Delta m}$$

Up till 1977, a unique unit of measurement for absorbed dosage was the rad, which is defined as 1 Rad = 100 erg g^{-1}. Rad is also the plural unit; for instance, 1 Rad or 20 Rad. Despite the introduction of the gray (Gy), a new special unit, the rad is still commonly utilized. The definition of gray is 1J deposited in 1 kg. 1 J kg^{-1} equals 1 Gy. In contemporary writing, gray is gradually replacing the Rad, and I shall make an effort to employ it consistently throughout this essay.

Since 1 Gy = 100 Rad, it is easy to convert between the rad and the gray since 1 rad = 1 cGy. Consequently, the centigray has become a common tool for scientific communication among radiation experts.

2.2.3 Radioactivity

Radioactivity defined as the occurrence of spontaneous nuclear changes within atoms that are unstable, leading to the creation of new elements. These transitions are distinguished by many mechanisms, such as the emission of alpha particles, the emission of beta particles and positrons, and the capture of orbital electrons. There's a chance that gamma radiation will be released in conjunction with any of these processes. Nuclear factors alone dictate the radioactivity and radioactive properties of nuclides; the radionuclide's chemical and physical states have no bearing on these properties. The radioactive characteristics of atoms are inherently unalterable and distinct from the specific radionuclides. The specific mechanism of radioactive transformation is contingent upon the amount of energy accessible for the transition process. It depends on two things: (1) the type of nuclear instability, that is, whether the

neutron-to-proton ratio is too high or too low for the nuclide under study; and (2) the mass-energy correspondence between the parent nucleus, and daughter nucleus, and released particle.

2.2.4 Decay Constant

For a radioactive nuclide in a particular energy state, the decay constant, denoted by λ, is the product of the change in the time (dt) interval and the change in the probability (d_P) of a nucleus undergoing a spontaneous nuclear transition from that state:

$$\lambda = \frac{dp}{dt}$$

The reciprocal of time, or t^{-1}, is used to describe the dimensionality of the decay constant.

2.2.5 Gamma Rays

X-rays and gamma rays are examples of electromagnetic radiation, which are photons with enough energy to cause ionization. X-rays and gamma rays have comparable physical characteristics. However, it has been customary to refer to ionizing photons generated in "machines" as X-rays, while ionizing photons emitted from radioactive sources are conventionally referred to as gamma rays.

2.2.6 Characteristic X-rays

The solar system atomic model possesses distinct qualities, wherein electrons orbit the nucleus with specific radii that correspond to discrete energy levels. The model possesses several virtues, including its ability to provide straightforward explanations for the transfer of energy to matter through processes like excitation and ionization. It also provides insights into processes such as the creation of characteristic X-rays and the photoelectric effect. Numerous

electron volts of excitation of outer electrons have been shown to give birth to the optical and ultraviolet spectra of various elements. Furthermore, the spectral lines correspond to the energy disparities between these excited states. The energy disparities across primary levels experience a significant increase as additional electron shells are included. Electron energy levels in elements with significant atomic numbers may reach tens of thousands of electron volts. For lead (Pb), the difference in energy between the K and L electron shells is 72,000 electron volts (eV). Figure 2.2 shows what happens when a photon with an energy higher than 87.95 keV interacts with the K electron. The electron is then released from the atom, leaving a space in the K shell. Simultaneously, an outer electron undergoes a transition to occupy the previously unoccupied energy level created by the ejection of the photoelectron. In the event of this occurrence, a photon is discharged, with an energy equivalent to the disparity between the initial and ultimate energy states, as stipulated by the following equation . When an electron moves from the L to the K energy levels in the instance of the lead (Pb) atom, a photon is released. The quantum energy associated with this emitted photon is measured to be 72,000 electron volts (eV). An X-ray is any photon with enough energy. Because of the unique energy differences between electron orbits that are unique to various atoms, the photon produced in this way is known as a characteristic X-ray. These X-rays, which represent these variations, are considered "characteristic" of the elements from which they originate. The aforementioned procedure is iterated until all the internal electron orbits are completely replenished. One may speculate that the first transition comes from the M level or perhaps from the outermost electronic orbit. The L shell is considered the most probable source of the initial electronic transition. When such an occurrence takes place, the resultant X-ray is referred to as a K_{α} photon. A K_{β} photon is produced whenever an electron moves from the M level to the K level. When an electron transitions from the M level to fill the vacancy in the L orbit, it produces an

X-ray known as Lα. Similarly, when an electron initially in the N level fills the L vacancy, it generates an X-ray referred to as L_β. The term "fluorescent radiation" is often used to refer to the characteristic X-rays that are emitted as a result of irradiating materials with X-rays. The utilization of characteristic radiation serves as a valuable tool for analytical chemists in the process of identifying unknown elements. The health physicist places significant attention on characteristic radiation, particularly in situations where radiation absorbers and high atomic numbered materials may emit fluorescent radiation due to the ejection of inner electrons.

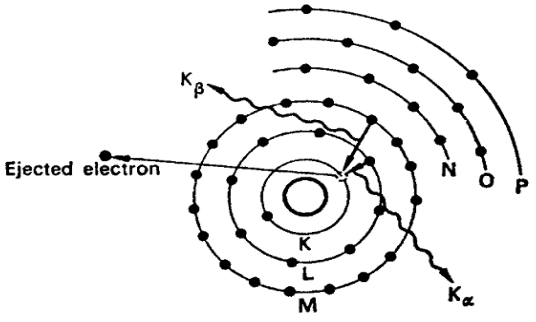

Fig. 2.1 Schematic representation of the origin of characteristic X-rays [1].

An X-ray photon with particular characteristics may come into contact with another electron in the atom and cause that electron to be expelled. The subsequent emitted electron is commonly referred to as an Auger electron. The Auger electron may come from an orbit outside of the original photoelectron's orbit or from the same orbit. The following is the formula for calculating an Auger electron's (E_{kA}) kinetic energy:

$$E_{kA} = \varphi_i - 2\varphi_o,$$

where φ_i = binding energy of the inner orbit and φ_o = binding energy of the outer orbit.

2.2.7 Interaction of Radiation with Matter

The interaction between radiation and substances holds significant importance from both theoretical and practical perspectives. This encounter can be analyzed from multiple perspectives. When a substance is exposed to radiation, it has the potential to undergo alterations in its properties. Because of the numerous developments in nuclear engineering, the use of radioactive isotopes, and the development of elementary particle accelerators, there has been a great deal of interest in researching the effects of radiation on materials used in electronic devices and control systems in recent years.

The dynamics of the interaction processes are contingent upon the characteristics of the incoming particles or photons, including their type and energy. An illustration of this concept is the electromagnetic spectrum, which encompasses a wide range of frequencies spanning multiple decades. The circumstances are analogous to those of particles that possess an electric charge. The energy spectrum spans from sub-electron volt (eV) levels to 10^{20} eV, exemplified by ultra-high energy cosmic rays. Throughout a gas medium, ion pairs—that is, electrons and positive ions—are formed as a result of the energy dissipation process. These pairs then split and travel throughout the medium. In general, the formation of an ion pair necessitates an energy input of approximately 30 electron volts (eV). In semiconductors, the medium is found to have a greater density, and the production of an electron-hole pair requires an energy input of around 3.6 electron volts (eV). Materials are much more vulnerable to the effects of ionizing radiation of many kinds, including gamma rays, α and β particles, neutrons, and X-rays. These interactions may be categorized as nuclear reactions, inelastic scattering, or elastic scattering based on the properties and energy level of the incoming radiation [Tareev, 1979; Turner, 2007].

During the process of radioactive decay, particles or rays are emitted with a specific energy level, and it is possible for these emissions to possess either a charge or no charge. After being discharged, each of these entities interacts with their surroundings, sending energy into the medium until they run out of energy altogether. As things stand, it is clear that these energy transfers will have a substantial impact on radiation biology, radiation shielding, radiation detection, and almost every other area of radiation protection.

The main processes by which radiation interacts with matter are:

- Ionization
- Excitation
- Capture

Fundamental processes like ionization and excitation are important in many different kinds of radiation and contact situations. Reactions resulting from the interaction of specific radiation types in certain conditions give rise to significant consequences, which shall now examined. One may conceptualize certain radiation interactions as akin to "billiard ball" collisions, specifically characterized by elastic scattering alone. When examining the interaction between a moving particle with mass M and a stationary particle with mass m, it is possible to determine the maximum amount of energy that may be transmitted during a single collision. This can be achieved by applying the principles of conservation of energy and momentum, assuming a "head on" collision scenario. Let us consider a scenario where particle M possesses an initial velocity denoted as V prior to a collision, and subsequently acquires a new velocity denoted as

V_1 after the impact. Particle m exhibited a state of rest prior to the collision, assuming a relative

perspective within the context of this interaction. Though most particles, including orbiting electrons, would normally have some kind of motion, it is important to keep this in mind. After the collision, particle m acquired a velocity denoted as v. Subsequently, by adhering to the principles of energy and momentum conservation, it can be deduced that:

$$\frac{MV^2}{2} = \frac{{MV_1}^2}{2} + \frac{mv^2}{2}$$

$$MV = MV_1 + mv$$

Solving 2nd equation for *v*, thus $v = (MV - MV_1)/m$, if this is substitute into 1st equation, thus $V_1 = \frac{(M-m)v}{M+m}$

The maximum energy that may be transmitted in a single collision is provided as follows if it's applied for V1:

$$Q_{max} = \frac{MV^2}{2} - \frac{MV_1^2}{2} = \frac{4MmE}{(M+m)^2}$$

2.2.8 Interaction of Gamma-Rays with Matter

The process by which gamma radiation interacts with matter will be reviewed in this paragraph to understand the features of a gamma spectrum that arise from interactions between the detector and its surroundings. Compton scattering, pair formation, and photoelectric absorption are the main interaction processes used in radiation measurements. In each of the aforementioned scenarios, there is a phenomenon wherein the energy of gamma-ray photons is partially or fully transferred to electrons, resulting in the production of unbound electrons. As these electrons traverse through the material, they undergo deceleration, leading to the

formation of electron-ion or electron-hole pairs. To explain the features seen in a gamma spectrum arising from interactions taking place inside the detector and its surrounding environment, this paragraph will provide a summary of the process by which gamma radiation interacts with matter. Compton scattering, pair formation, and photoelectric absorption are the main interaction processes used in radiation measurements. In each of the aforementioned scenarios, there is a phenomenon wherein the energy of gamma-ray photons is partially or fully transferred to electrons, resulting in the production of unbound electrons. As these electrons traverse through the material, they undergo deceleration, leading to the formation of electron-ion or electron-hole pairs.

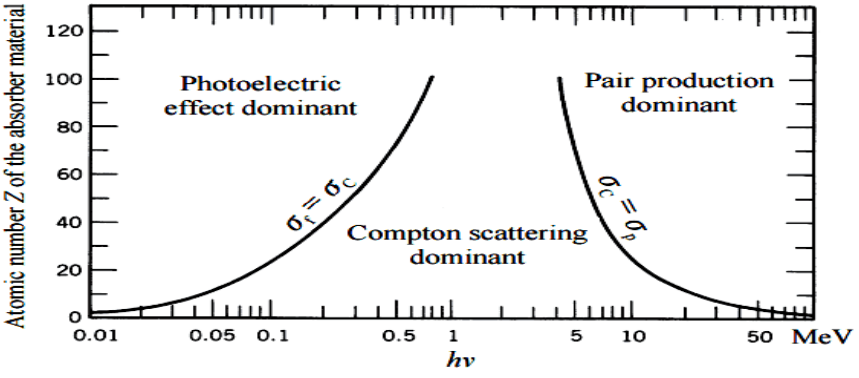

Fig 2.2 The relative importance of various processes of gamma radiation interaction with matter [1].

2.2.9 Photoelectric Absorption

The phenomenon of photoelectric absorption takes place when a gamma-ray photon interacts with an electron that is bonded within an atom. When the energy of a gamma-ray surpasses the binding energy associated with that specific shell, an electron may be ejected from its shell, which is typically the innermost K-shell (see Figure 2.2). If there isn't enough energy to release a K electron, it's possible that L or M electrons will be released instead. The

phenomena described causes the photoelectric absorption spectra to exhibit sharp discontinuities that correspond to the binding energies of the electron shells K, L, and M. These discontinuities are referred to as K, L, or M edges. The gamma-ray outcome is completely absorbed, resulting in the electron acquiring a kinetic energy denoted as E_e:

$$E_e = E_\gamma - E_b$$

Here, E_b stands for the energy binding an electron to its shell, while E_γ stands for the energy related to γ-rays. It is often noted in the context of momentum conservation that the recoiling atom has to save a very small amount of energy while an electron is being ejected.

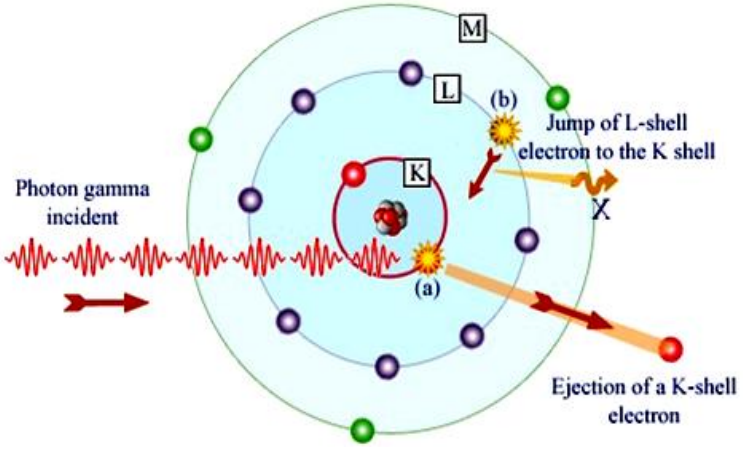

Fig. 2.3 The mechanism of photoelectric absorption [6].

This entity possesses negligible dimensions and can be disregarded in the context of practical applications. With an excess energy of Eb, the atom stays excited and eventually returns to equilibrium, either by filling the vacancy left by the photoelectron with an electron from the outer shell with a greater energy or by redistributing the excitation energy among the atom's remaining electrons. This process leads to the emission of a characteristic X-ray known as X-ray fluorescence (Figure 2.3). Subsequently, the X-ray has the potential to undergo

photoelectric absorption, potentially resulting in the emission of more X-rays. This process may continue iteratively until the entire energy of the γ-ray is absorbed. The energy level from which the electron is emitted is contingent upon the energy of the γ-ray. The K electron is the most probable candidate for ejection.

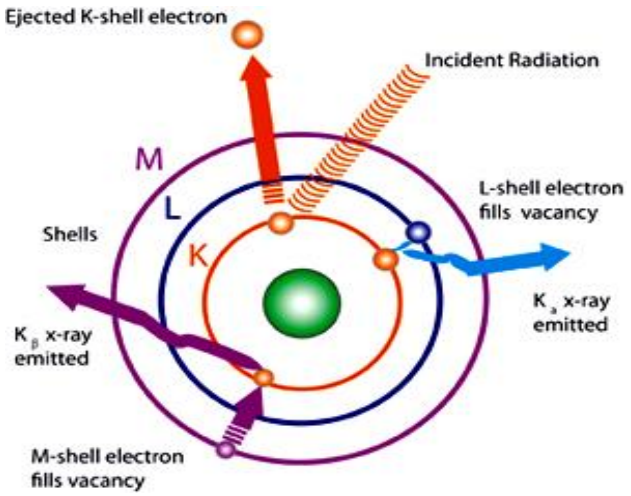

Fig. 2.4 The emission of fluorescent X-rays [6].

When a K electron cannot be released due to insufficient energy, L or M electrons will be emitted in its stead. The discontinuities in the photoelectric absorption curves result from this. The binding energies that correlate to the electron shells are where these absorption edges occur. The probability that a photon will undergo photoelectric absorption is expressed as a cross-section (τ), and it rises via a complicated connection as the energy of the γ-ray (E) grows and the absorber's atomic number (Z) lowers:

$$\tau \approx Z^n/E_\gamma^m$$

Therefore, n and m fall between 3 and 5 depending on energy. The photoelectric attenuation coefficient, or μ_{PE}, may be derived from the appropriate cross-section in the following way:

$$\mu_{PE}(m^{-1}) = \tau \times \rho \times N_A/A$$

Where ρ is the density of the absorbing material, A its average atomic mass, and N_A is Avogadro's number.

2.2.10 Compton Scattering

In this scenario, the photon will selectively impart portions of its energy to an electron. A further gamma photon with a lower energy level absorbs the remaining energy. The newly emitted photon is referred to as being dispersed, as it will undergo a change in trajectory. The electron that is expelled from the atom induces ionization in a manner analogous to that of a beta particle.

In contrast to the photoelectric effect, this process:

- The transfer of energy from a photon to an electron is only partial and
- The procedure solely involves the electrons that are virtually unbound and located in the outer orbitals.

The photon undergoes scattering at an angle θ relative to the incident line (Figure 2.4) and experiences a loss in energy as it continues its trajectory. The phenomena of Compton scattering may be adequately described by thinking of the photon with energy E as a wave of wavelength λ:

$$\lambda - \lambda_o = \frac{h}{mc}(1 - \cos\theta)$$

$$\text{Where, } E_\lambda = h\upsilon = \frac{hc}{\lambda}$$

Once the scattering angle θ is established, one may compute using conventional mechanics:

- The angular orientation of the electron's trajectory and
- The allocation of energy between the electron and the scattered photon occurs in a specific ratio.

The greatest energy that a photon may transmit to an electron is when θ = 180˚, or when the photon is directly scattered backward. Even so, it is still less than the entire energy that a single photon in a photoelectric interaction is capable of transferring. You can choose any value between 0˚ and 180˚for the scattering angle. The quantity of energy delivered to the electron decreases with decreasing angle. When a photon "grazes" an electron (θ = 0˚), no energy is transferred.

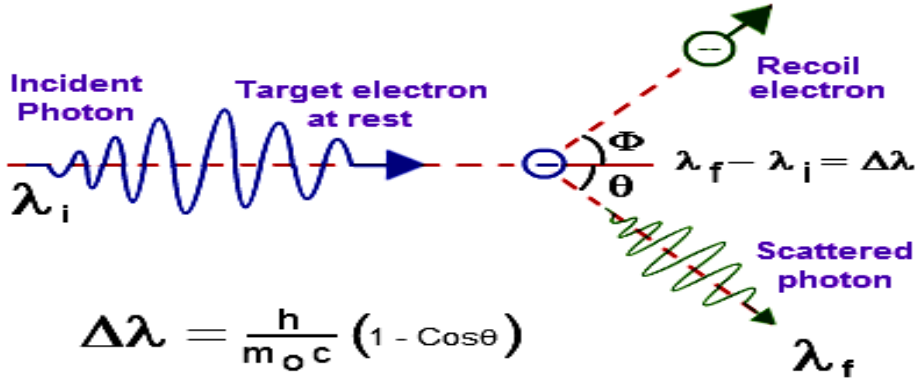

Fig. 2.5 Compton scattering process.

The probability of a Compton interaction has a positive correlation with the absorber's atomic number and a negative correlation with the incoming photon's energy. To summarize, this may be expressed as follows:

$$\text{Probability of Compton scattering} = k\frac{Z}{A}$$

With regard to the geometric configurations often used for sample counting, an intriguing scenario arises:

The sample is placed close to the detector within a strong shield, usually composed of lead. The detector therefore "sees" photons that are directly emitted from the sample and a lesser quantity that were all reflected by the absorber by around 180 ˚.

This backscattering produces photons with almost the same energy regardless of the photons' energy affecting the lead shield. The pulse height spectrum's low energy area displays a board peak that represents the backscattered photons.

2.2.11 Pair Production

High-energy gamma photons may sometimes divide into two types of electrons: positive and negative. The positive electron is known as a positron. Its referred that interaction as pair creation. The theory of relativity, which holds that "matter" and "energy" are two distinct forms of the same thing, can be used to explain the effect. The equation states that a quantity of energy E can be created from a particle of mass m and vice versa:

$E = mc^2$; where c is the speed of light.

Some implications of this idea include the following: pair of creations Two separate particles with the same mass but opposing electrical charges are created from a photon's energy E.

The two particles split the extra energy between them as kinetic energy:

$$E_\gamma = (m_+ + m_-)c^2 + \frac{1}{2}(m_+ + m_-)v^2$$

Electrons are the two particles that are involved. The negative electron is one, and the positive

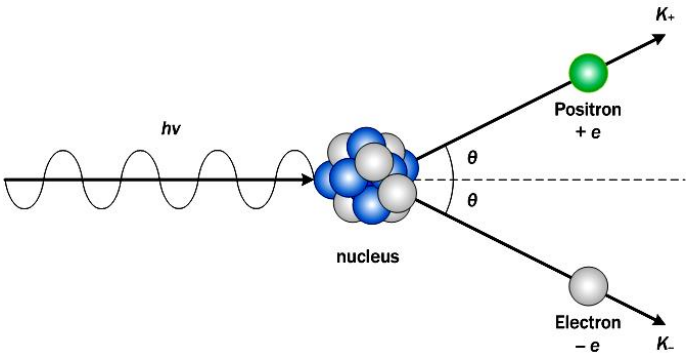

Fig. 2.6 Pair production process.

electron, often known as the positron, is the other. Although it has the opposite electrical charge from the negative electron, it shares the same mass and nuclear characteristics. Sometimes, to distinguish between a negative and a positive electron, one uses the term negatron.

The quantity of energy equivalent to the mass of an electron or positron may be found using the Einstein equation (9.11×10^{-28} g). It is equal to 511 KeV for a single particle and 1022 KeV for a positron-negatron pair. Consequently, the above equation may be written as:

$$E_\gamma = 1022\ \text{KeV} + \frac{1}{2}\,(m_+ + m_-)v^2$$

When at rest, the positron is not a stable particle. Similar to how a negatron loses energy by interaction with electrons in absorbing materials, a positron that has been formed through pair formation will also lose energy. However, a nuclear reaction happens when it loses all of its kinetic energy and is unable to survive in the presence of additional electrons. Two photons with a combined energy of 511 KeV are produced in this reaction when a pair of positrons and negatrons destroy one another. The annihilation can take place not only with the electron generated during pair creation, but also between the positron and any other electron.

Two photons are involved in the reaction in order to maintain momentum. It is exemplified by:

$$\beta_+ + \beta_- \rightarrow \gamma_1 + \gamma_2 \text{ and } E_{\gamma_1} = E_{\gamma_2} = 511 \text{ KeV}$$

Only when the incident photon's energy is high enough (>1022 Kev) to provide a positron and negatron pair's mass, can a pair be produced. Practically speaking, it only matters for photon energies greater than 1.5 MeV. Pair formation is more likely to happen at higher photon energies.

2.2.12 Ion Irradiation

In order to cause changes in a target material's physical, structural, and transport properties, ion irradiation involves the application of energetic ions to the substance. This method of material modification is interesting since it is non-equilibrium in nature and sensitive to a variety of materials, such as metals, semiconductors, ceramics, insulators, polymers, and biological samples.

The principles of ion-solid interaction have become more important over the past ten years. The increased necessity to use beams to change materials for particular applications is the cause of this trend. Ion beam and solid interaction occurs in a non-equilibrium manner. Two essentially independent processes cause an energetic ion to lose energy when it enters a target:

(i) Inelastic collisions between the matter's atomic electrons and highly charged, energetic ions [electronic energy loss $(dE/dx)_e$] and

(ii) Atomic nuclei of the matter's elastic scattering [nuclear energy loss $(dE/dx)_n$].

Through excitation and ionization of the surrounding electrons in an inelastic collision (cross-section 10^{-16} cm^2), energy is transferred from the projectile to the matter atom. Each collision loses a different amount of electronic energy, ranging from a few eV/Å to a few keV/Å. This

is the primary method for energy transfer to the material that modifies its properties in nanoparticles traveling at velocities similar to the electron's Bohr velocity. The target material's electrical, thermal, and structural characteristics, the projectile ion's mass, and the irradiation settings all affect the type of change. [17].

2.3 SURVEY OF EARLIER WORKS

Veena et al. [18] studied $Ni_{1-x}Zn_xFe_{2-y}Dy_yO_4$ (x = 0.0, 0.2, 0.4, 0.6, 0.8, 1.0; y = (0.0 and 0.1) nano ferrites that were created using a creative, practical, and affordable combustion process. A study using X-ray diffraction was conducted to verify the phase development. With an increase in Zn content and a drop in Dy^{3+} ion content, the lattice constant rises. The range of the typical crystallite size was 11–31 nm. The ac conductivity increases and the dielectric constant and loss tangent decrease with increasing frequency. Electrical conduction in the samples is hindered by the addition of Dy^{3+} ions. The frequency range of 5–7 MHz was where the resonance peaks were seen. The production of Fe^{2+} ions in irradiated samples caused enhancements in the lattice constant, crystallite size, and dielectric properties. When the amount of Dy in the sample increases, the peak height decreases and the peak location shifts to a lower frequency in radiation-exposed samples. The conduction mechanism caused by the grain boundary is revealed by the complicated impedance analysis.

S.T. Assar et al. [7] investigated Ni–Cu–Zn and Mg–Cu–Zn nanoferrites having the formula $Ni_{0.35}Cu_{0.15}Zn_{0.5}Fe_2O_4$ and (b) $Mg_{0.35}Cu_{0.15}Zn_{0.5}Fe_2O_4$ respectively, have been effectively synthesized using the auto-combustion method of citrate precursor. The effects of 1 Mrad and 2 Mrad doses of ^{60}Co radioactive source on the structural, specific magnetic, and electrical properties have been studied using γ-ray exposure.

The XRD data show that, for Ni–Cu–Zn ferrite samples, the ordered portions of the crystallites, or grains, are lost as the irradiation dosage rises, resulting in an increase in the disordered grain border area. In addition to increasing porosity, specific surface area, and microstrain, this results in a reduction in densification. As a consequence of increased unit cell stacking and well-ordered grain sizes, the Mg–Cu–Zn ferrite samples exhibit an increase in crystallite sizes. This suggests that irradiation energy has a role in these processes, which ultimately lead to increased densification and reduced porosity, specific surface area, and microstrain. In addition, some Fe^{3+} (0.67 Å) and Fe^{2+} (0.76 Å) were converted.

The primary factor influencing the customization of the samples' magnetic characteristics is cation redistribution, which is responsible for the observed increases in saturation and remnant magnetization following irradiation. The distribution of cations in the studied samples has been proposed so that the experimental and theoretical magnetic moment values are the same and grow with increasing magnetization. A comparison between the experimental and theoretical estimates of the lattice constant provides more support for the validity of the hypothesized cation distribution, since they correspond rather well. Similar to Ni-Cu-Zn ferrite samples, the DC conductivity values of Mg-Cu-Zn ferrite samples also increase when the γ-ray irradiation dose increases, but at higher levels due to the extra influence of their microstructures beyond cation redistribution.

Plots of the samples using Cole–Cole (Z″ vs. Z') reveal two overlapping incomplete semicircles. The first occurs at low frequencies and is caused by the conduction of the grain boundaries, where it is impossible to determine their electrical parameters. The second occurs at high frequencies and is caused by the conduction of the grains, which have higher capacitance and lower resistance than the grain boundaries and exhibit a significant change in

their values in response to the dose of radiation. The semicircular Cole–Cole plots of (M vs. M') guarantee that the electric stiffness of the samples under investigation is the primary characteristic both before and after the irradiation dose. Ultimately, it can be said that while samples of $Ni_{0.35}$ $Cu_{0.15}Zn_{0.5}Fe_2O_4$ exhibit greater magnetization and resistivity than samples of $Mg_{0.35}Cu_{0.15}Zn_{0.5}Fe_2O_4$ under extremely high γ-ray irradiation, both can be regarded as promising candidates to be used in the production of MLCIs because of their balanced behavior under higher irradiation exposure.

All of the study's samples, according to Karim et al. [19], had a single-phase cubic spinel structure. All significant peaks were visible in samples of Ni–Zn ferrites that were both irradiated and unirradiated. Because of ion-induced disorder, the irradiation samples in both systems show lesser intensities and larger line broadening. The presence of stable induced flaws at room temperature in the Ni–Zn ferrite following gamma-ray Co^{60} irradiation is demonstrated by the results. It is anticipated that these faults will result from the interaction of two or more factors. It has been noted that the particle sizes inferred from the 311 XRD peak broadening for both irradiated and unirradiated materials are (10–24) μm and (52–30) μm, respectively. The partial creation of ferrimagnetic centers, cation rearrangement in the lattice, and ion-induced disorder are responsible for the observed increase in the saturation magnetic moment and Curie temperature following irradiation.

According to a study by Kee-Nam Choo et al. [20] The primary use of HANARO's irradiation facilities has user-requested nuclear material irradiation testing. Even though the bulk of irradiation experiments at HANARO have been related to national R&D related to nuclear power, the necessity for neutron irradiation of electromagnetic materials is rapidly increasing. Taking the lessons learned from HANARO, KAERI is constructing the KIJANG research

reactor (KJRR), which will increase the country's capability to supply radioisotopes and shield thermal neutrons for use in irradiation facilities like the FNI facility for fast neutron irradiation and the NTD facilities for large-scale power semiconductor production. It is possible to effectively study the different impacts of heat and fast neutron irradiations on the properties of electro-magnetic materials by using the NTD and FNI capabilities of the KJRR reactor. There appears to be a lot of potential for the basis for neutron irradiation-based material research in the field of electromagnetic material research.

According to M.A. Ahmed et al. [8], $MnFe_2O_4$ nano ferrite was created using the citrate approach in a single spinel form with cubic symmetry and without the need for further heat treatment. Gamma irradiation decreases the particle size (L) of the $MnFe_2O_4$ nano ferrite while increasing its unit cell volume, TC, and room temperature values of χM, $\varepsilon^{/}$, tanδ, and σ. The unit cell volume of the nano ferrites is reduced by neutron irradiation, although its L, TC, and room temperature values of χ_M, $\varepsilon^{/}$, tanδ, and σ rise. When the nano ferrite is exposed to laser light, its L and χ_M drop, but its unit cell volume, TC, room temperature values of $\varepsilon^{/}$, tanδ, and σ increase. Lastly, the alterations in the behavior of irradiation nanoferrites are detected by means of their dielectric and magnetic characteristics. On the basis of this data, it can be said that the micro ferrite is verified to be used in the detection of nuclear contamination and has the greatest potential for use as a radiation detector in industrial and technical applications.

Dogra et al. [21] looked at changes in the dielectric properties of Mg-Mn ferrite replaced with Al^{3+} by 50 MeV Li^{3+}. The XRD studies revealed that the ion irradiation had changed the electrical characteristics, resulting in compressive strain. The dielectric constant $\varepsilon^{/}$ of unirradiated samples was found to be dispersed due to Maxwell-Wagner type interfacial polarization and Koops's hypothesis.

In situ monitoring of the electrical resistance of a thin coating of $Li_{0.25}Mg_{0.5}Mn_{0.1}Fe_{2.15}O_4$ micro ferrite exposed to 190 MeV Au^{14+} ions was studied by Ghosh et al. [22]. To look into the quick changes in the electrical properties of the film brought on by heavy ions, an in situ measurement of electrical resistance utilizing two probe techniques was carried out. It was shown that following exposure to radiation at a flux of 1×10^{13} ions/cm^2, the resistivity value drops sharply from (1.5×10^8 to 1×10^5) Ω cm.

Chhantbar et al. [23] investigated the impact of 50 MeV Li^{3+} ion irradiation on the structural and magnetic characteristics of Ti^{4+} substituted $Li_{0.5}Al_{0.1}Fe_{2.4}O_4$. Using magnetization, ^{57}Fe Mössbauer spectroscopy, and x-ray diffraction (XRD), the effects of 50 MeV Li^{3+} ion irradiation on the structural and magnetic behavior of polycrystalline samples of the spinel ferrite system were examined. Following SHI irradiation, the Mössbauer spectra showed central amplification, which was explained by the paramagnetic centers the irradiation produced. According to XRD and Mössbauer Lorentzian intensity analysis, the partial creation of paramagnetic centers and cation rearrangement in the lattice were responsible for the decrease in saturation magnetic moment that was seen following SHI irradiation. The origin of the central amplification seen in the irradiated samples' Mössbauer spectra can be traced to the creation of localized paramagnetic centers rather than amorphization.

The impact of 100 MeV Si^{7+} irradiation on the structural and magnetic characteristics of $Mg_{0.95}Mn_{0.05}Fe_2O_4$ nanoparticles was investigated by Kumar et al. [24]. After irradiation, a little increase in particle size was discovered. Super

paramagnetic relaxation effects were seen in both the irradiated and clean samples using room temperature Mössbauer spectroscopy. There were no appreciable changes in the room temperature Mössbauer spectra after ion irradiation. At room temperature, the samples were all superparamagnetic, but at 5 K, they all showed distinct magnetic ordering. Based on the magnetization analyses conducted on the samples exposed to radiation, it was determined that there was an enhancement in saturation magnetization. This was described in terms of single-domain particles growing under the influence of coercivity, where the absence of domain walls prevented the magnetization from reversing. The surface state pinning of domains was released and the nanoparticles' magnetism was enhanced by radiation.

Darwish et al. [25] as well as Hemeda et al. [26] studied the effect of gamma ray irradiation using a ^{60}Co source on the structure and the electrical properties of Co-Zn ferrites. A shift in XRD peaks was observed following irradiation. The γ-radiation induced a conversion of ferric ions to ferrous ions, resulting in an increase in their radius from 0.59 Å to 0.69 Å. The crystal's size was augmented using the process of γ-irradiation. The phenomena that has been seen may be explained by the increase in ferrous ion concentration at the octahedral sites due to exposure to γ-radiation. This increase in concentration leads to an expansion of the lattice parameter and an enhancement of polarization under the influence of an electric field. It was observed that the diffusion coefficient exhibited an increase subsequent to gamma irradiation across all concentrations of Zn^{2+}. The effect reported may be explained by the metal ions being displaced by radiation

from their initial locations. This displacement results in the creation of lattice vacancies, which subsequently lead to an increase in the diffusion coefficient.

The impact of gamma irradiation on the structure and diffusion coefficient of Co-Zn-Mn ferrites was studied by Hamada et al. [16] and Dalal et al. [27]. This observation suggests a minor deviation from the ideal cubic form. The irradiated samples exhibited an increase in the diffusion coefficient of electrons. The irradiation spectra also revealed the presence of a defect that was generated during exposure to γ-irradiation. The radiation that was applied during the first stage of temperature rise caused the activation energy of hopping electrons to drop. The jumping holes in this system were the majority carriers at high temperatures.

A comparable investigation on Co-Zn-Ce-Fe_2O_4 ferrites was reported by Ateia et al. [28]. According to the research, the unirradiated samples had bigger crystallites than the irradiated ones. In contrast to the unirradiated samples, the calculated micro strain values in the irradiated samples were greater. Moreover, it was noted that after the irradiation procedure, the dielectric constant ε′ increased. The observed rise in ε′ could be attributed to the formation of Fe^{2+} ions following irradiation, as well as the creation of vacancies at various depths that serve as trapping sites.

The impact of gamma irradiation on the structural and electrical characteristics of the Mg-Ti-Er_2-Fe_2O_4 system was investigated by Ahmed et al. [29]. A discernible alteration in the XRD peaks was seen subsequent to the irradiation process. The observed phenomenon can be attributed to the alteration of the Fe^{2+}/Fe^{3+} ratio on

the octahedral sites as a result of the interaction between γ-irradiation and Fe^{2+}, leading to the conversion of Fe^{2+} to Fe^{3+} by the process of $\gamma + Fe^{2+} \leftrightarrow Fe^{3+} + e-$. As a result, there was a reduction in the size of the crystals. Furthermore, it is seen that there was a significant rise in the dielectric constant. Displacement may cause some distortion to the tetrahedral sites, which would cause anions to migrate away from the closest tetrahedral cations. The conductivity exhibited a positive correlation with the increase in γ-dose. The observed rise in σ can be attributed to the corresponding increase in the Fe^{2+}/Fe^{3+} ratio on the octahedral sites, which is a direct result of the hopping process. The activation energy measurements exhibited a reduction as the dose increased.

By using γ-irradiation, Okasha et al. [30] were able to enhance the magnetization of Mg-Mn micro ferrite. The ionization of ferric ions, which have a lower ionic radius, into ferrous ions, which have a bigger ionic radius, is responsible for the observed expansion in lattice constant for the irradiated materials. The presence of superparamagnetic behavior was demonstrated by the absence of hysteresis, saturation, remanence, and coercivity at a higher applied magnetic field of 6 kOe. Furthermore, the saturation magnetization (M_s) values of the irradiated samples were found to be higher compared to those of the unirradiated samples. The internal cation disorder and the impact of the tiny particle surface effect were used to explain this phenomenon.

The effects of gamma irradiation on the distribution of cations, the structural integrity, and the magnetic characteristics of Ni-Zn ferrites were studied by Karim et al. [31]. The analysis revealed that the XRD peak positions exhibited a shift

towards higher 2θ values, accompanied by a drop in peak intensities. Furthermore, there was an observed increase in the diameter of the peaks when comparing the irradiated samples to the unirradiated ones. After irradiation, there was a drop observed in the value of the lattice constant. The observed phenomenon can be ascribed to the presence of lattice vacancies that arise as a result of irradiation, leading to deformation and divergence from the cubic structure of the spinel. The cation distributions showed that the redistribution of cations in the A and B-sites was initiated. The observed alteration in the distribution of cations can be ascribed to the generation of Fe^{2+} ions at octahedral sites subsequent to irradiation. An rise in both the saturation magnetic moment and Curie temperature was seen after irradiation. The observed phenomenon can be attributed to the partial production of ferrimagnetic centers and the rearrangement of cations within the lattice, as well as the introduction of disorder generated by ions.

Cu-Mg-Zn ferrites were made using the gel auto-combustion approach by Zhenxing et al. [32]. The investigation focused on examining the impact of Cu ions on the electromagnetic characteristics. The study revealed that the synthesized powders demonstrated a notable level of sintering activity, enabling the ferrite phase to undergo sintering at temperatures below 950 °C. The evaluated samples exhibited favorable electromagnetic characteristics and refined microstructures, rendering them acceptable materials for high-performance multilayer chip inductors. The electromagnetic parameters that are influenced by the copper content include dielectric constant, dielectric loss tangent, dc resistivity, quality factor, and initial permeability.

For the first time, $ZnFe_2O_4$, $Mg_{0.5}Zn_{0.5}Fe_2O_4$, and $Mg_{0.2}Cu_{0.2}Zn_{0.62}Fe_{1.98}O_{3.99}$ powder were made using flame spray synthesis by Vital et al. [33]. It was discovered that the flame process produced the crystalline spinel particles with a primary particle size of (6–13) nm. The precursor's molarity, flow rate of the atomizing gas, and particle and crystallite sizes were all related. Without the use of any sintering additives, a sintered density of 5.05 g/cm^3 was attained after 2 hrs. of fire at 900 ^oC. The sintered Mg–Cu–Zn ferrite nano powder compacts had saturation magnetization of 80 emu g^{-1} and permeability of μ = 600 at 1 MHz.

The production of nano-sized PbO-added Cu-Mg-Zn ferrites using microwave hydrothermal method was studied by Raju et al. [34]. After an hour of treatment, it was discovered that the samples produced at a low temperature of 160 oC had particle sizes in the range of 10–20 nm with high surface area. Investigations were conducted into how the additive concentration affected the saturation magnetization, electrical resistivity, initial permeability, and sintered density. The results were compared to those produced using the traditional ceramic process. Improvements in electrical resistivity, permeability, and sintered density were observed upon the addition of PbO.

B. M. Sahanashree et al [35] were investigated Nanosized $Co_{1-x}Zn_xFe_{2-y}Nd_yO_4$ ferrites were synthesized by combustion method. A ^{60}Co gamma ray source was used to irradiate each sample. Spinel ferrite phase development was verified by XRD analysis. The average crystallite size ranged from 12 to 39 nm, and for irradiation samples, it rose to 15 to 40 nm. As frequency increased, ac conductivity increased while the dielectric constant and dielectric loss dropped. It has been

noted that impedance characteristics vary similarly with zinc content. Nd3+ is added to the samples, which enhances electrical conductivity and prevents it following irradiation. Multiple electrical responses were suggested by complex impedance spectra.

The fabrication of nanostructured Ni-Zn-Dy nano ferrites by burning was studied by M. Veena et al. [36]. The XRD patterns and infrared spectra verified that cubic spinel ferrite had formed. With Dy substitution, the lattice parameter lowers, and with Zn^{2+} concentration, it rises. The graphs between logσ and 1000/T nano ferrites show two zones, which correspond to paramagnetic and ferrimagnetic behavior at Curie temperature (T_C). The paramagnetic regions exhibited higher activation energies compared to the ferrimagnetic regions. The T_c values were clearly moved to lower temperatures when the concentration of Dy ions and Zn^{2+} ions increased. The nano Zn ferrite's ferrimagnetic characteristic was demonstrated by the magnetic investigation. It was discovered that samples with Dy^{3+} ions substituted had lower magnetic parameter values. Upon gamma irradiation, decreases in the x-ray density and crystallite size were noted, along with an increase in the lattice parameter. The lattice's tetrahedral and octahedral site cation rearrangement is responsible for the seen improvement of DC conductivity and magnetic properties upon irradiation.

CHAPTER 3: MATERIALS AND METHODOLOGY

3.1 MATERIALS

Sol-gel synthesis was used to synthesize Ni-Cu-Cd nanoparticles with the compositional formulas respectively. The raw materials that will be utilized include $Ni(NO_3)_2.6H_2O$, $Cu(NO_3)_2.3H_2O$, $Al(NO_3)_3.9H_2O$, $Cd(NO_3)_2.4H_2O$, and $Fe(NO_3)_3.9H_2O$ in their analytical grade. The components' stoichiometric mixes are dissolved in pure ethanol. The above solution is kept in water bath at a temperature of 70 °C and stirred constantly using a

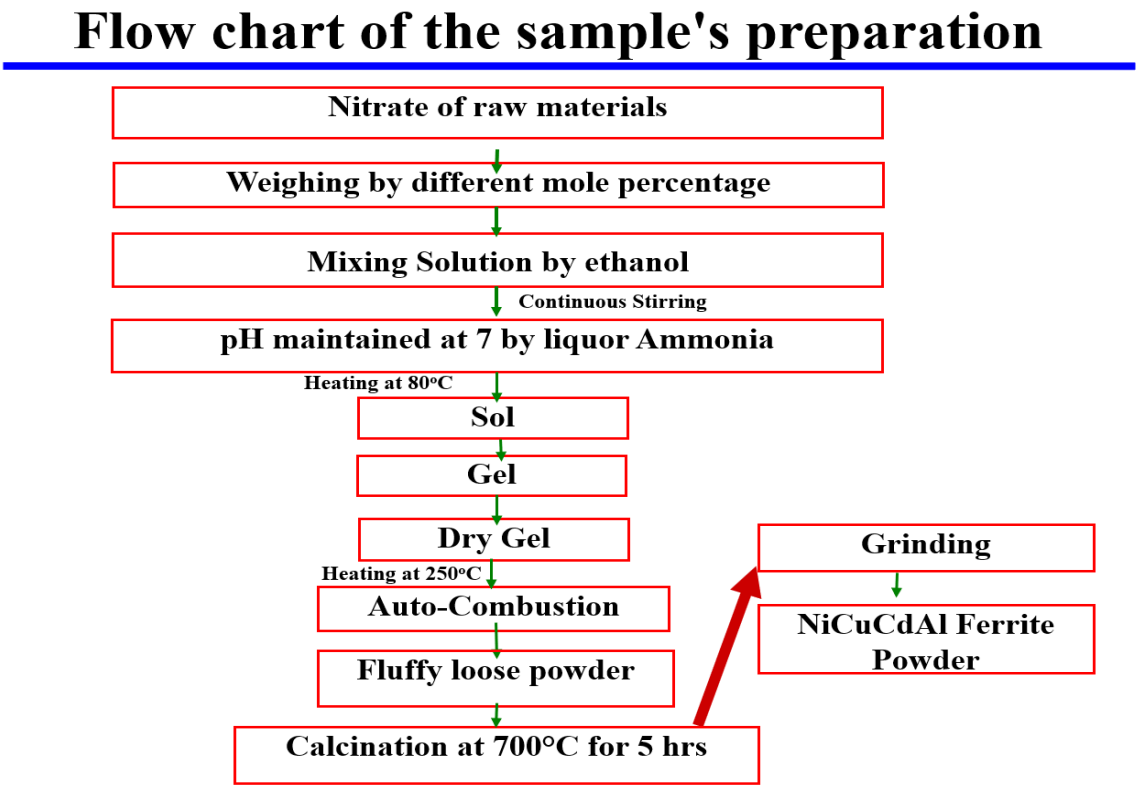

magnetic stirrer until gel formation takes place. Liquor ammonia will be used to keep the pH of the solution at 7. This gel is then annealed for five hours at 200 ℃. During this heating

Fig. 3 Flow chart of the sample's preparation

phase, the gel will continue to self-ignite until it burns entirely, becoming a fluffy, loose powder.The powder is then heated for five hours at 700 ºC each to remove any last traces of organic material from the sample. For electric measurements, the samples are pressed into pellets in the form of a circular disc in order to construct a parallel plate capacitor geometry with ferrite material serving as the dielectric medium. The pellets' opposite faces are then covered with silver paste as two probe contact.

The study involved the use of Ni-Cu-Cd-Al nano ferrite samples for gamma irradiation. These samples were placed in the center of a Co^{60} gamma irradiator with an energy level of approximately 1.3325 MeV. Two different doses, 1MRad and 3MRad, were administered. During long irradiation, all the samples and standards were placed together in the same irradiation vial and irradiated simultaneously. Following the irradiation process, the vial that had undergone irradiation was subsequently placed within a lead container for a duration of two days. This was carried out to lessen the possible radiation hazard and to permit the decay of short-lived radionuclides. The irradiation source is situated at the Institute of Nuclear Science and Technology (INST), AERE, Savar, which is under the purview of the Bangladesh Atomic Energy Commission (BAEC).

The specimens' XRD patterns are acquired subsequently to their exposure to gamma (γ) irradiation. The measurements were conducted using a D8 advance X-ray Diffractometer equipped with CuKα radiation ($\lambda = 0.15418$ nm). The instrument has operated at the Process

Development Centre, Bangladesh Council of Scientific and Industrial Research (BSCIR), located in Dhaka. The calculation of the average L was performed using Scherrer's formula [37]. L is the particle size in nanometers (nm), β is the full width at half maximum, λ is the radiation wavelength, and θ is the diffraction angle. This formula may be found by solving $L = 0.89\lambda/\beta\cos\theta$. At the Material Science Division of the Atomic Energy Commission (AEC) in Dhaka, the magnetic properties of the current samples has examined using the Micro Sense EV9 Vibrating Sample Magnetometer (VSM). Electrical and dielectric transport characteristics were measured at room temperature in the 20 Hz–10 MHz frequency range. The two sides of the pellet has covered with silver paste and checked to make sure there was enough electrical contact. Furthermore, at Chittagong University of Engineering and Technology (CUET) in Chittagong, Bangladesh, the Postgraduate Laboratory of the Department of Physics conducted dielectric properties, impedance measurements and modulus spectroscopy using a computer-controlled Wayne Kerr Precision Impedance Analyzer (6520A, UK).

3.2 EXPERIMENTAL TECHNIQUES

This chapter provides a description of fundamental experimental techniques employed for the measurement of lattice parameters and frequency-dependent dielectric characteristics of ferrite nanoparticles. The physical characterization of the samples was conducted using X-ray diffraction (XRD). A Vibrating Sample Magnetometer (VSM) was utilized to conduct the DC magnetization measurement. The measurement of transport characteristics was conducted using two probe techniques employing an impedance analyzer. The dielectric measurements were conducted with a custom-designed sample holder and an impedance analyzer. The present study also includes a comprehensive examination of impedance and modulus spectroscopy.

3.2.1 X-ray Diffraction Analysis

One method that provides important insights into the crystal structure is XRD. Cu-Kα radiation with a wavelength of λ = 0.15418 nm has used in an X-ray diffractometer for the structural characterization. Within the powder, a multitude of grains exhibit arbitrary orientations. For specific grains, it is expected that most of the unique atomic planes would align parallel to the surface in the case of random orientations. Consequently, the act of scanning from various angles would be linked to distinct atomic spacing. The powdered sample was carefully placed onto a sample stage in order to undergo irradiation by X-ray radiation.

The X-ray powder diffractogram may provide the following details:

- The quality and verification of the prepared samples
- The spacing between the planes of reflection, denoted as d_{hkl}, is a crucial parameter to consider.
- The intensities of the reflections
- The unit cell dimensions and lattice type.

An electronic detector was placed on the other side of the sample, opposite the X-ray tube, to determine if diffracted X-rays were present. The sample was then systematically rotated across various Bragg's angles. The goniometer was utilized to monitor the angular position (θ), while the detector recorded the X-rays discovered in counts per second (counts/sec). Subsequently, this data was transmitted to the computer.

For each sample, XRD patterns were acquired in order to identify the phases and ascertain their preferred orientations. The data collection was performed throughout a 2θ range of 15–60º, with a step size of 0.01º. Plotting the X-ray intensity (measured in counts per second) against

the angle theta (2θ) produced a graphical depiction after the sample scanning procedure was finished. The 2θ values corresponding to each diffraction peak were subsequently transformed into d-spacing values by applying Bragg's equation, which states that nλ = 2d Sinθ, where n represents the order of diffraction [38].

The formula that was provided was used to calculate the lattice parameter for each peak in each sample. [39]:

$$a = d\sqrt{h^2 + k^2 + l^2}\ ;$$

The crystal plane indices are represented by the variables h, k, and l. The exact lattice parameter for every sample was determined using the Nelson-Riley method. The expression [40] represents the Nelson-Riley function F (θ):

$$F(\theta) = \frac{1}{2}[(cos^2\theta/\sin\theta) + (cos^2\theta/\theta)]$$

Plotting the lattice constant 'a' values for each peak in a sample against the variable F (θ) creates a graphic. A least square fit approach is used to determine the precise lattice parameter 'a_o'. The real lattice parameter of the desired sample is represented by the y-intercept of the least square fit straight line, or F(θ) = 0.

3.2.2 Crystallite Size Measurement

The determination of particle size holds significant importance in the context of ferrite nanoparticles. When fine particles are present, the X-ray diffraction (XRD) lines exhibit broadening, indicating a drop in particle size. This broadening phenomenon provides unequivocal evidence of the decrease in particle size. The full width at half maximum (FWHM) of the diffraction peaks is measured in order to determine the particle size. In the realm of

crystallography, a crystal is commonly regarded as achieving a state of perfection when its constituent atoms fully fill all lattice sites, hence exhibiting an absence of any imperfections within the crystal structure. The phenomenon of diffraction peak broadening can be primarily attributed to three key reasons. The broadening of peaks is observed as a result of reduced crystallite sizes, and so, an examination of peak broadening can be employed to ascertain the sizes of the crystallites, which in turn contribute to additional broadening in the diffraction peaks.The average size of the crystallites (D) in the samples was calculated using the linear intercept approach on nano-graphs [41]. Bragg's law describes the need for constructive interference, which strengthens X-ray scattering from a crystalline powder. An exact connection is found between the integral (n) number of X-ray wavelengths and the path difference of X-rays scattered from parallel crystalline surfaces spaced d apart. The crystallographic planes provide the reference point for measuring the diffraction angle. In the case of an infinite crystal, Bragg scattering manifests itself at distinct values of the scattering angle that adhere to the Bragg condition. Consequently, the resulting Bragg peaks can be described as a Dirac delta function. In the case of crystals with finite dimensions, the observed peaks exhibit a broadening effect that spans a range of angles.

In order to gain insight into the phenomenon of fine particle widening, it will be examined a finite crystal with a thickness denoted as D = md, where m represents an integer and d represents the distance between crystal planes. Consequently, within the given thickness D_{311}, there exist m planes.

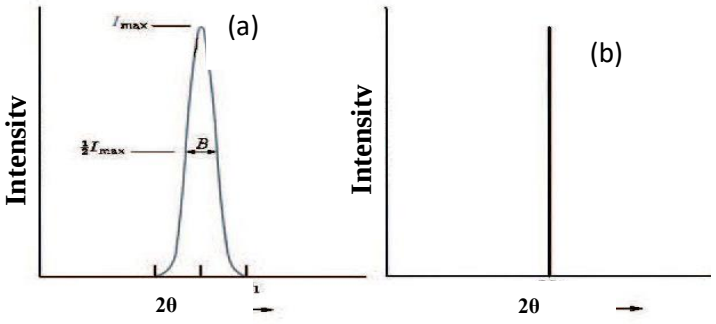

Fig. 3.1 Effect of fine particle size on diffraction curves (Schematic): (a). small particle size and (b) large particle size.

The full width at half maximum (FWHM) or breadth of the peaks is indicated as follows when looking at Fig. 4.5, where the widened Bragg peak terminates at and starts at an angle,

$$\beta = \frac{1}{2}\left(2\theta_1 - 2\theta_2\right) = \left(\theta_1 - \theta_2\right)$$

When examining the route differences for both angles θ_1 and θ_2, in the case of X-ray propagation through the entire thickness of the crystal, it is important to take into account these variations. The measurement of breadth is often expressed in radians. Instead of using the separation between adjacent planes to describe the path difference equations for the two angles, one may use the overall thickness of the crystal.

These equations are given as follows:

$2\ D_{311} \sin\theta_1 = (m+1)\lambda$ $2\ D_{311} \sin\theta_2 = (m-1)\lambda$

By subtraction: $D_{311}(sin\theta_1 - sin\theta_2) = \lambda$

or, $2D_{311}\ cos\left(\frac{\theta_1+\theta_2}{2}\right) \sin\left(\frac{\theta_1-\theta_2}{2}\right)$

But θ_1 and θ_2 are both very nearly equal to θ so that $\theta_1 + \theta_2 \approx 2\theta$ and $\sin\left(\frac{\theta_1-\theta_2}{2}\right) \approx \left(\frac{\theta_1-\theta_2}{2}\right)$. So the equation can be written as:

$$2D_{311}\, cos\left(\frac{2\theta}{2}\right)\left(\frac{\theta_1-\theta_2}{2}\right) = \lambda$$

or, $2D_{311}\, cos\theta\, \left(\frac{\theta_1-\theta_2}{2}\right) = \lambda$

From above, $D\beta cos\theta = \lambda$

or, $D_{311} = \frac{\lambda}{\beta cos\theta}$

A more exact empirical treatment yields: $D_{xrd} = \frac{0.9\lambda}{\beta cos\theta}$

The formula in question is commonly referred to as Scherrer's formula. This technique is employed to determine the particle size of minuscule crystals by analyzing the measured width of their diffraction curves. The contribution of instrument-induced line widening was subtracted from the measured peak width prior to the calculation of the crystallite size, as per the following mathematical expression:

$$B^2 = B_{meas}^2 - B_{equip}^2$$

where B_{meas} = measured full width at half maximum from peak, B_{equip}= instrumental broadening.

3.2.3 Wayne Kerr Precision Impedance Analyzer

For accurate measurement and study of impedance in a wide variety of electronic devices, including parts, circuits, and both electronic and non-electronic materials, the Wayne Kerr impedance analyzer is a valuable tool. Additionally, this instrument holds significant utility in the realms of circuit design and development, as well as research and development pertaining to both electronic and non-electronic materials.

- The device offers precise measurements across a broad range of impedance and frequency, spanning from 20 Hz to 15 MHz;
- It also provides robust impedance analysis capabilities;
- Additionally, it is user-friendly and offers flexible networking options with personal computers.

The complex impedance Z of the coil [42] can be expressed as follows: $Z = R + jX$;

Where the R represents the resistive part and the reactive part is X.

3.2.4 Magnetic Hysteresis Analysis

Saturation is a term used to describe a state in which a substance or medium has reached its maximum capacity or concentration. It is The magnetization of the ferrite specimen has been measured by measuring the force it experiences in a field gradient. The measurement was conducted with a vibrating sample magnetometer (VSM) manufactured by Micro Sense, specifically the EV9 model, as depicted in Figure 3.3. The fundamental concept underlying VSM involves quantifying the electromotive force generated by a magnetic specimen when subjected to controlled vibrations at a consistent frequency within a static and homogeneous

magnetic field. A minute quantity of nanocrystalline minerals, weighing approximately 10-11 mg, was carefully measured and secured within the sample container to prevent any internal motion. The VSM was utilized at a magnetic field strength of 3 Tesla, with a vibration frequency of 82 Hertz. The calibration process involved the utilization of a nickel standard (in the form of a sphere) possessing a well-established magnetization value (specifically, M_s = 6.92 emu at 5 kOe).The EV9 VSM is capable of generating magnetic fields of up to 26 kOe inside a sample spacing of 5 mm. When the temperature chamber is installed, the maximum magnetic field strength achievable is 21.5 kOe. The Vector Space Model (VSM) demonstrated the capability to generate magnetic fields with intensities reaching 1 Tesla. The Vector Space Model VSM exhibited the capability to identify magnetic moments with a sensitivity as low as 0.5 electromagnetic units (emu).

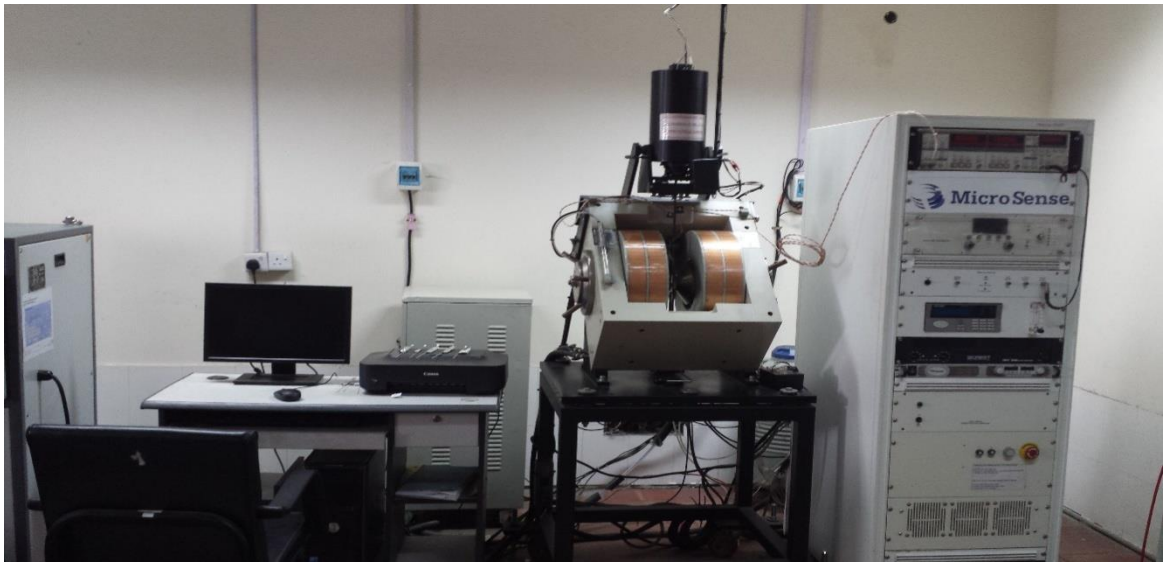

Fig. 3.2 Vibrating Sample Magnetometer at Atomic Energy Commission, Dhaka.

3.2.5 Complex Dielectric Measurements

There are many categories of polarizations, and each has a physical process that explains them. Three primary types of polarizations are known to exist: electronic, ionic, and orientation polarizations. When an insulator is subjected to an external electric field, the relative positions of the electrons and nuclei within the atoms are altered, leading to the emergence of induced dipole moments. These induced dipole moments contribute to the phenomenon of electronic polarization. In cases where the electrons of a molecule's atoms are not shared in a symmetrical manner, there will be an eccentric displacement of the electron-clouds towards the more strongly binding atom. Consequently, the ions obtain charges of contrasting polarity. In the event of an external electric field, the ions with net charges will undergo a displacement in their equilibrium positions.

A secondary type of an induced dipole moment results from the displacement of charged ions or groups of ions relative to one another. This effect represents the ionic polarization shown by the different components of a molecule, which leads to the existence of dipole moments that are always present even in the absence of an external electric field. These kinds of dipoles experience a torque in the presence of an electric field, which helps to align them with the field's direction. As a result, the occurrence of an orientation polarization, also known as dipole polarization, may arise. The three mechanisms responsible for polarization arise from the presence of charges that are confined within atoms, molecules, or the solid structure. Furthermore, it is common for there to be charge carriers present inside the dielectric material that are capable of migrating over certain distances.

Using a computer-controlled Wayne Kerr impedance analyzer (model 6500B), the electrical and dielectric transmission properties were evaluated. The pellet-shaped samples were

thoroughly polished to remove any surface roughness and other oxide contamination that could have happened during the sintering process before conducting electrical and dielectric tests. In addition, silver paint was applied to each pellet's two surfaces to function as the contact material. The Wayne Kerr impedance analyzer was utilized to perform tests of dielectric properties, alternating current (AC) conductivity, and impedance (both real and imaginary components) at ambient temperature. The formula [43-44] was employed to compute the real component of the dielectric constant.

$$\varepsilon' = \frac{Cd}{\varepsilon_0 A}$$

In this instance, C stands for the pellet's capacitance, expressed in Farads (F), and l for the pellet's thickness, expressed in meters (m). ε_0 is the constant of permittivity for free space, and A is the size of the cross section of the chosen paint region, measured in square meters (m^2).

The sample's imaginary component of the dielectric constant (ε'') was computed using the following relation: $\varepsilon'' = \varepsilon' \times tan\delta;$ where tanδ represents the dielectric loss tangent.

The calculation of the alternating current (AC) conductivity has performed using the formula $\sigma_{ac} = d/(A*R_{ac})$, where R_{ac} represents the AC resistance. The equation provided can be expressed as;

$$\sigma\ (\omega, T) = \sigma_{dc}(T) + \sigma_{ac}(\omega, T),$$

where σ_{dc} represents the direct current conductivity and is only dependent on temperature. The second term, denoted as σ_{ac}, represents the AC conductivity. This parameter is influenced by both temperature and frequency. The frequency-dependent electrical conductivity, denoted as σ_{ac}, can be mathematically described using the empirical formula*:* $\sigma_{ac}(\omega, T) = A\omega^n$. In this

equation, A and n are constants that are influenced by both temperature and composition. The constant n is dimensionless, while the constant A has units of electrical conductivity (σ_{ac}).

3.2.6 Impedance Spectroscopy

An very efficient method for analyzing the electrical properties of complex oxides is complex impedance spectroscopy. The technique offers several key benefits. First of all, it involves simple electrical measurements that are amenable to automation. Second, any kind of electrode may be used to carry out these measures. Thirdly, the obtained results often exhibit correlations with various sample properties, including composition, microstructure, defects, dielectric properties, chemical reactions, and more. Finally, in most polycrystalline materials, the approach clearly distinguishes between the resistance of individual grains and that of grain borders. AC measurements are commonly conducted using a Wheatstone-bridge-based apparatus, such as an impedance analyzer or LCR meter. This apparatus allows for the measurement and balancing of the resistance (R) and capacitance (C) of the sample by adjusting variable resistors and capacitors. Impedance spectroscopy is a technique used to determine the impedance magnitude (|Z|) and the phase difference (θ) between voltage and current as a function of frequency for a specific sample. The analysis of the data involves the construction of an impedance plot, which is a complex plane where the imaginary component of the impedance $Z^{/}=|Z|\cos\theta$ is plotted against the real part $Z^{//}=|Z|\sin\theta$. Using a linear scale, the impedance plot is used to analyze the same circuit in the following way. The impedance plot of a pure resistor is represented as a singular point located on the real axis, while the impedance plot of a pure capacitor is depicted as a linear trajectory that aligns with the imaginary axis. The expression for the impedance of a parallel RC combination is given by the following equation,

$$Z^{*} = Z^{/} - jZ^{//} = R /(1+j\omega RC)$$

After simplification, one gets

$$(Z^{/} - R/2)^2 + Z^{//2} = (R/2)^2,$$

which represents the equation of a circle with radius R/2 and center at (R/2, 0). Consequently, when plotting Z' against $Z^{//}$ (as a parametric function of Ω), a semicircle with a radius of R/2 will be obtained. The time constant of the simple circuit is formally defined as the product of the R and the C, denoted as t = RC. It may also be expressed as the reciprocal of the angular frequency (ω_m), given by $t = 1/\omega_m$. The aforementioned statement pertains to the relaxation time of the sample, with the characteristic frequency being situated near the apex of the semi-circle. In an ideal polycrystalline specimen, the impedance plot demonstrates distinct features: a high-frequency arc representing the bulk characteristics of the sample, a low-frequency arc indicating the behavior of the grain boundaries, and a spike at the lowest frequency associated with the electrode effect.

3.2.7 Modulus Spectroscopy

The study of complex modulus spectroscopy is a valuable and informative approach employed in materials research. It provides essential insights into the distribution parameters of several nano areas inside nano-crystalline materials, including grain, grain boundary, and electrode interface. The identification of various mechanisms associated with relaxation and AC conduction can be achieved by graphing the modulus at different frequencies on a complex plane. This approach proves to be highly efficient in distinguishing the influences of grain and grain boundary effects. Moreover, the utilization of modulus spectroscopy plots proves to be particularly advantageous in the differentiation of components exhibiting comparable

resistance yet varying capacitance. Another benefit of utilizing the electric modulus formalism is the mitigation of the electrode effect. The utilization of complex electric modulus formalism has been chosen as a result of the aforementioned factors. The investigation of dielectric relaxation has been conducted using the formalism of complex modulus M^*. The real and imaginary components of the electric modulus were derived from the impedance data using the corresponding mathematical relationship:

$$M^{/} = \varepsilon' / (\varepsilon'^2 + \varepsilon''^2) = \omega C_0 Z'' \text{ and } M^{//} = \varepsilon'' / (\varepsilon'^2 + \varepsilon''^2) = \omega C_0 Z'.$$

CHAPTER 4: RESULTS AND DISCUSSION

4.1 GENERAL

The study results are shown in this part along with discussion of their significance. Within the framework of the study goals, the findings are interpreted such as XRD as well as Rietveld Refinement, Magnetization, Dielectric Studies, Modulus Studies and, Dynamic Conductivity. Every segment is thoroughly discussed with proper scientific reference.

4.2 STRUCTURAL ANALYSIS

4.2.1 XRD

The ferrite sample's XRD patterns for compositions $Ni_{0.5}Cu_{0.2}Cd_{0.3}Fe_{2-x}Al_xO_4$ after irradiating with 1 MRad and 3 MRad are represented in Fig. 1(a) and Fig. 1(b) respectively. Single spinel phase has been shown in XRD patterns in each of every investigated sample after gamma irradiation. A comparison of sample spectra after gamma irradiation shows the relative peak intensities of peaks (400) and (511) decrease after gamma irradiation. The peaks of XRD correspond to the increase of diffraction planes indicated as (222), (440), and (511). In addition, it is also noticed that the peak intensity of (440) is less than the peak intensity of (311). As a result, the (440) plane becomes denser than the (311) plane after coming out of gamma irradiation. In addition, the intensity of peaks (400) and (440) decreased after gamma irradiation, and the peak (220) also decreased.

Patterns for all the samples show allowed lines of reflection without any extra peaks in the XRD pattern. Thus these patterns depict the spinel structure of the cubic single phase for all investigated samples. Literatures report a similar trend for lattice [45- 47]. In Fig. 4.1 which

represent after irradiation patterns reveals the transition of the peak at 2θ values with the decrease in intensities of peaks. However, the improved width has been observed in unirradiated samples [48].

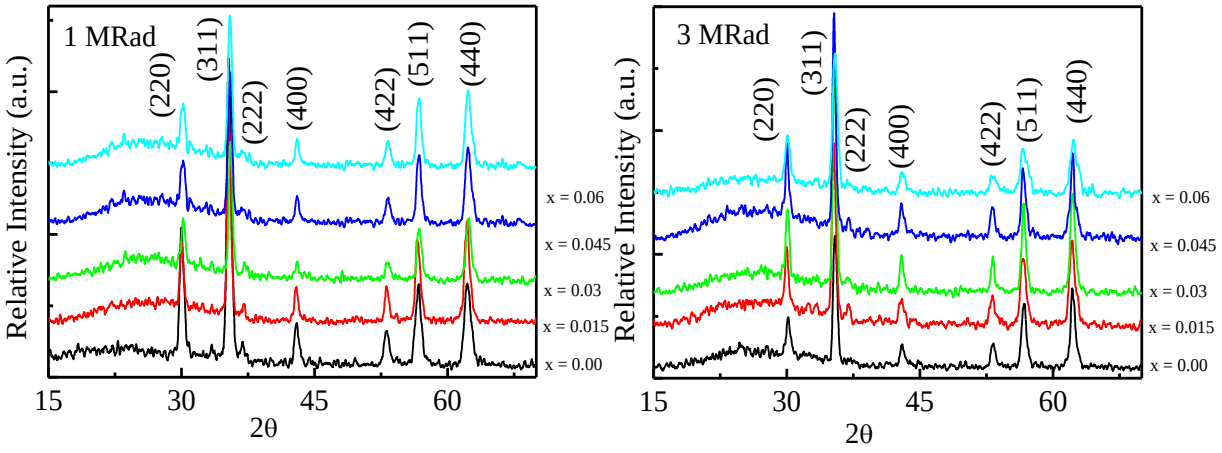

Fig. 4.1 The XRD patterns of the irradiated samples of (a) 1 MRad and (b) 3 MRad γ irradiation of $Ni_{0.5}Cu_{0.2}Cd_{0.3}Fe_{2-x}Al_xO_4$.

Due to distortion and deviation after irradiation from the structure of cubic spinel, the generation of lattice vacancies occurs and decreases the lattice constant [49]. The distortion in a lattice structure and strain shrinkage might be another reason for the vacancies [50]. In the current case, an increase in lattice constant is observed. The mass increment imposes the increment of the lattice constant. For comparison, the resultant lattice constant and particle size for irradiated samples with two different doses are listed in Table 4.1.

Besides, other information that has been found from this investigation is that irradiation causes a decrease in particle size. It may be noted that high energy ions tend to penetrate along the beam trajectory of ions due to the irradiated ions. Hence material modification is the resultant

Table 4.1 Some structural data of the unirradiated and irradiated samples of the $Ni_{0.5}Cu_{0.2}Cd_{0.3}Fe_{2-x}Al_xO_4$ for gamma irradiation

Al content	1 MRad					3 MRad				
	0.00	0.015	0.03	0.045	0.06	0.00	0.015	0.03	0.045	0.06
From XRD										
Lattice parameter (a), Å	8.45454	8.44442	8.43629	8.42594	8.41952	8.47742	8.46611	8.46016	8.45617	8.44809
Particle size (t), nm	21	20	18	16	15	29	22	21	10	18
From Rietveld refinement										
Lattice parameter (Å)	8.4935	8.4959	8.4658	8.4633	8.4425	8.4471	8.4628	8.491	8.4582	8.4453
Volume $(Å)^3$	612.723	613.232	606.743	606.205	601.749	602.725	606.105	612.18	605.113	602.339
Crystallite size, nm	25	24.5	23	21	19	32	28	25	22	20
χ^2	1.58	1.59	1.43	1.91	1.85	1.47	1.55	1.72	1.7	1.53

Phase cubic spinel, *Space group* Fd-3 m

phenomenon that occurs during molecules spitting and pushing positional change of the atoms. The decrease in the average size of particles turns into partial amorphization and the generation of defects has occurred due to the loss of energy from radiation. These are done during the irradiation process.

The transition of ions from different interstitial positions results in the redistribution of cations. To ionize more, gamma irradiation collides with A ions and B ions. The migration can be given by,

$$Fe^{2+} \text{ to } Fe^{3+} \text{ as } Fe^{2+} + \text{irradiation} \longrightarrow Fe^{3+} + e^{-}.$$

As a result lattice parameter and particle size change [51, 52]. The formation of Fe^{3+} ions can be attributed to the gamma ray interaction process with the outer electrons in the lattice [18]. From Table 4.1, variations of the particle size for irradiation type are obtained. Radiation damage to the crystal lattice may produce permanent changes in ferrites' electrical and magnetic behaviour [54]. These changes influence total dose rate, dose absorbed in materials, and dose time. These data are essential to evaluate the

performance of ferrite in electronic components even cosmic radiation usage rather high accumulated dose in satellites and space craft's [55]. As a result, cluster pairs of vacancy are the expected formation. Moreover, the vacancy of cluster pairs has enhanced the disappearance of planes such as (222) and (533). From a closer perspective, a greater shift is evident in the plane of the unirradiated sample than in the gamma-irradiated sample. This implies that both ionization in spinels and damage displacement in spinels are produced by the radiation process [56]. On the other hand, cations of B sites are proposed only for vacancies [57]. In contrast, it is possible to exist A and B vacancies of cations at a time for the disorder [58]. It is possible to state that irradiation causes an increase in the spinel inversion and an increase in the lattice parameter. Hence the probable occurrence might be an increase in inversion in spinel and lattice lattice parameters due to gamma irradiation.

4.2.2 Rietveld Refinement

The data of irradiated nanoparticle samples are studied by the method of Rietveld refinement.

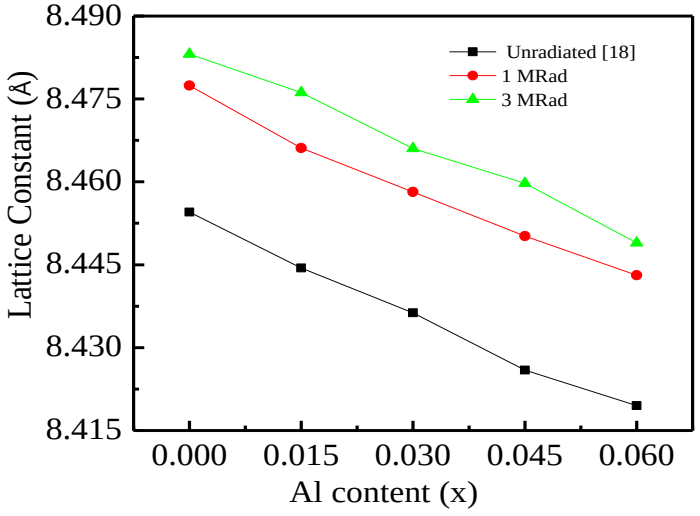

Fig. 4.2 Variation of lattice constant of irradiated sample of γ irradiation of $Ni_{0.5}Cu_{0.2}Cd_{0.3}Fe_{2-x}Al_xO_4$.

Fig. 4.3 and Fig. 4.4 are demonstrating the outcomes for samples after refining through Rietveld refinement. The goodness of fit for the Rietveld refinement output is indicated by χ^2. If the obtained value of χ^2 is less than 1 then the fitting is considered the best fitting approach [59]. According to that fact, all outcomes are have been to have a χ^2 value less than 1 and thus show the best fit. Moreover, the fitting was done for the space group Fd-3m and pseudo Voigt function.

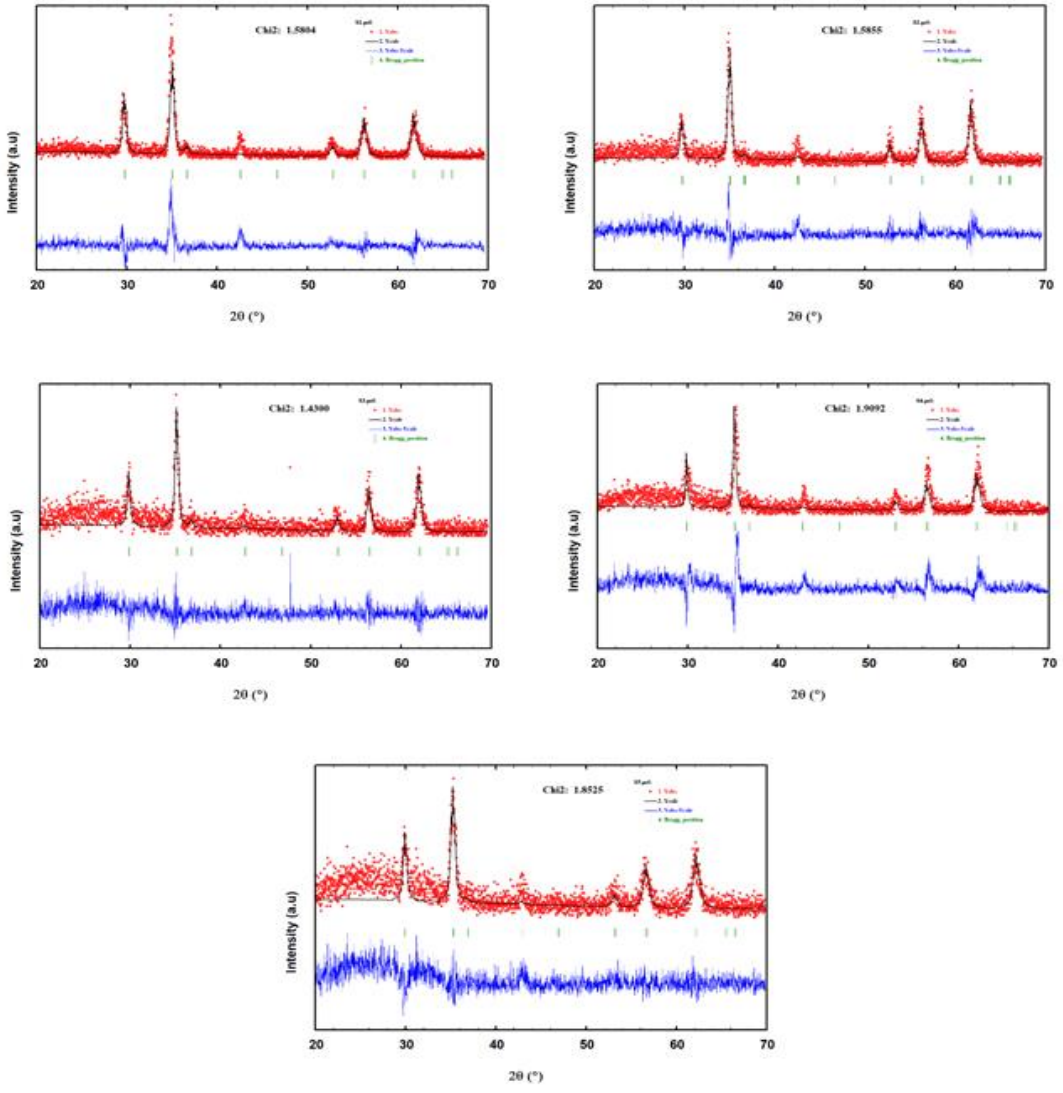

Fig. 4.3 Rietveld refinement of XRD patterns of $Ni_{0.5}Cu_{0.2}Cd_{0.3}Fe_{2-x}Al_xO_4$ due to 1 MRad γ irradiation.

The fitting parameters such as lattice parameters, volume, and χ^2 values are listed in Table 4.1 for the irradiated samples after irradiation of 1 MRad and 3 MRad. Table 1 shows that the lattice parameter, as well as volume of the samples, has been decreased with the increase in Al content in the 1 MRad irradiated compound. Similar patterns have been found of 3 MRad irradiation except for the sample with Al content 0.03. Compressive strains of the compound are responsible for the decay in size.

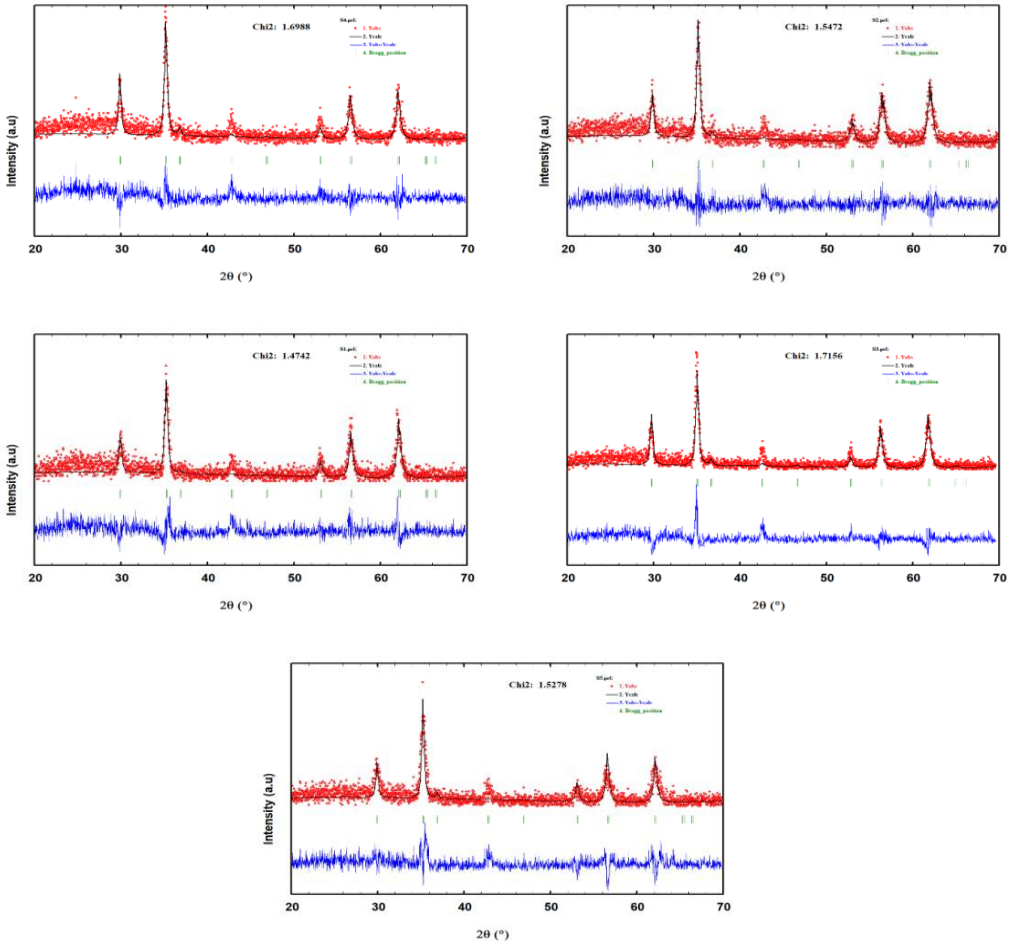

Fig. 4.4 Rietveld refinement of XRD patterns of $Ni_{0.5}Cu_{0.2}Cd_{0.3}Fe_{2-x}Al_xO_4$ due to 3 MRad γ irradiation.

4.2 MAGNETIC HYSTERESIS

Fig. 4.5 shows the magnetization M ($A.m^{-1}$) change with the applied magnetic field H(T) up to 1 T. consists both before gamma radiation and after the irradiation that is applied at room temperature for the investigated samples. The increase in magnetization is observed with the application of a magnetic field, which agrees with normal behavior. The spin motion of electrons and motion of orbital is considered the origin of magnetic properties and therefore magnetism of the materials. Due to electrons' magnetic moment, atomic magnetic moments and ionic magnetic moments are result.

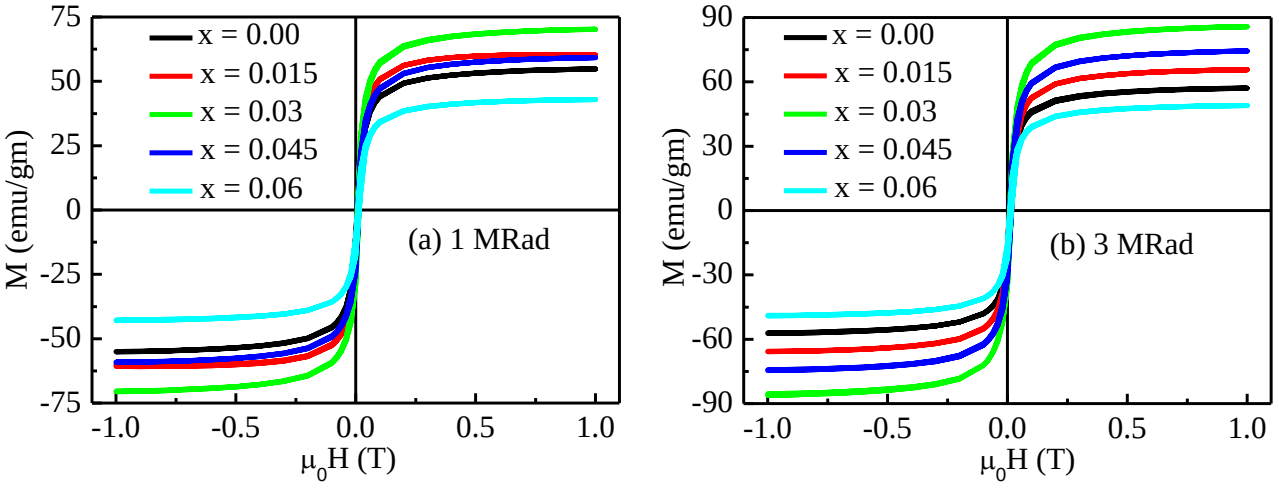

Fig. 4.5 Variation of M with H for (a) 1 MRad and (b) 3 MRad γ irradiation of $Ni_{0.5}Cu_{0.2}Cd_{0.3}Fe_{2-x}Al_xO_4$.

The magnetic behaviors of nanoparticles that are synthesized have been characterized through a VSM at room temperature with an applied field of 1.0 T (in $\mu_0 H$) for achieving saturation which is plotted in Fig. 4.5 (a). The various magnetizations (M) against the magnetic field (H) that have been applied at room temperature (27°C) for both before and after irradiation $Ni_{0.5}Cu_{0.2}Cd_{0.3}Fe_{2-x}Al_xO_4$ ferrite nanoparticles are shown in Fig. 4.5.

The increase of M for all compositions is found with the increment in $\mu_0 H$ near 0.25 T which is composition-dependent and after the application of field M shows slow rises and then it turns to saturation. The magnetization extrapolation determines saturation magnetization (M_s) which plots to $1/(\mu_0 H) = 0$. This type of variation in M_s with Cu^{2+} content could be explained based on exchange interaction along with cation distribution, as cation distributions over A-sites and B-sites influence ferrite nanoparticles magnetic properties. The magnetic characteristics of synthesized nanoparticles can be ascribed to the relative shiftiness of ions of ferromagnet for instance Ni^{2+} (2 μ_B), Fe^{3+} (5 μ_B), and lower magnetism of Cu^{2+} (1 μ_B) as a nonmagnetic shift of metal ions which occur in the occupied A-sites and B-sites. The cations are distributed on the A-site and B-site in a way like $(Ni_{0.7-x}^{2+} Cu_x^{2+} Fe_{1.3}^{3+})_B O_4^{2-}$ by considering the case where all cations are placed in their respective positions. Previous reports show similar findings such as Belavi et al [59] and Hemeda [61]. Also, the magnetic properties of the ferrites are expected to improve because Cu is a Jahn–Teller ion. As a result, lattice distortion has been improved which ultimately produces a strain of large size in ferrite lattice which is attributed to the enhancement of magnetization [62]. As shown in M vs H curve in Fig. 4.5, the coercivity of our synthesized ferrite nanoparticles is very low, which defines the samples as soft ferrites. Generally, the M_s of nanocrystalline ferrites are less than that of bulk ferrites, which is reflected in our study. The existence of smaller nano elements with morphological core-shell could be responsible for the lower magnitude of M_s. The nano particles is consisted of surface layer type spin-glass and core spins that are aligned with ferromagnetic nature. Therefore, smaller values of M_s due to the atomic symmetry of dissimilar types have occurred. The breaking of superior exchange bonds leads to disorder and canting in the spins of the surface layer.

Since the ferrite atoms accept the interactions of superexchange type, the above effects are probable. This leads to reducing the interaction between the exchange of A and B and decreases subsequently in M_s for the studied Ni-Cu-Cd ferrite nanoparticles. To get more accuracy, a theoretical process known as the law of approach to saturation (LAS) is applied to the positive parts of the DC magnetization data, and outputs are demonstrated in Fig. 4.6.

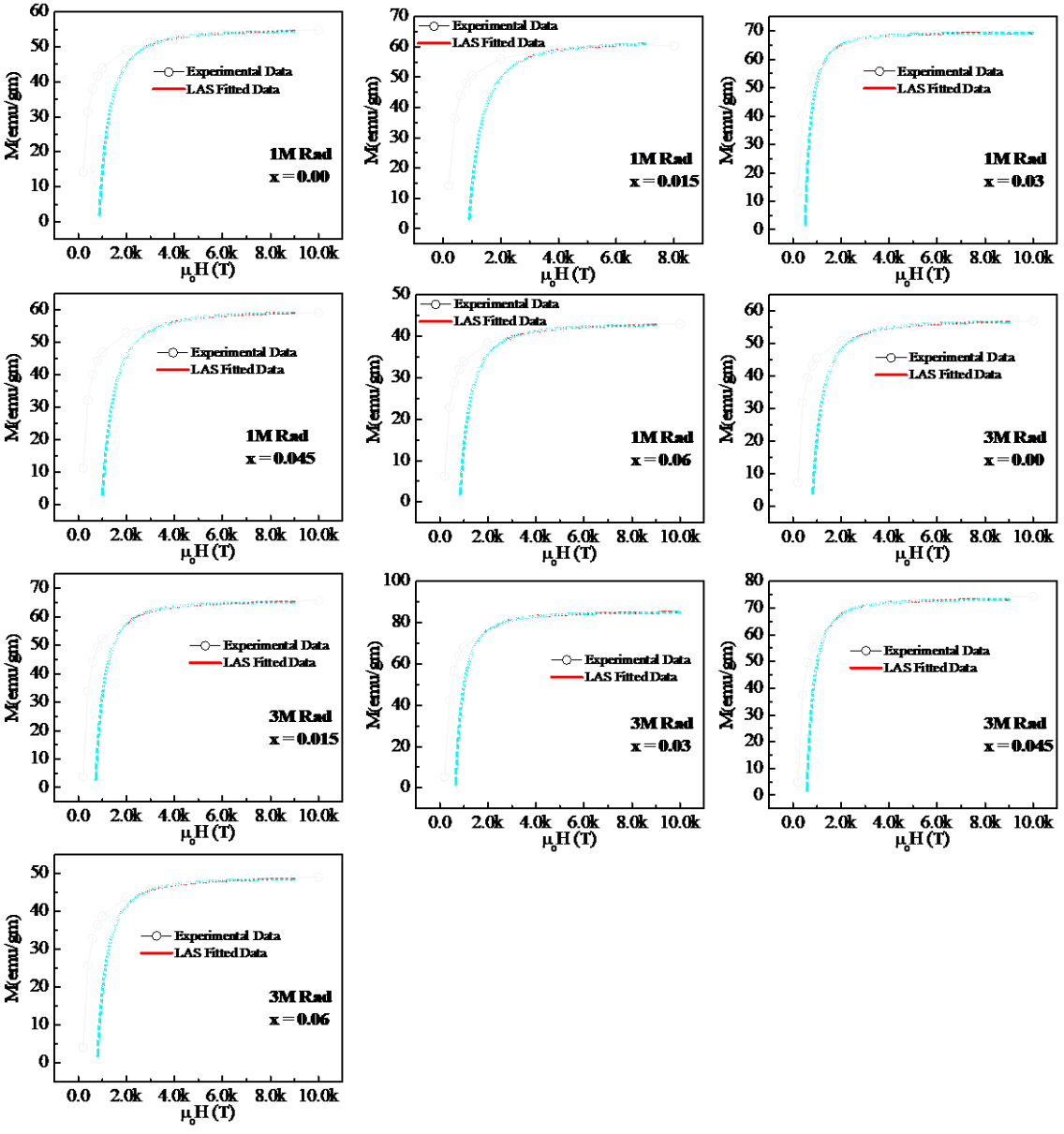

Fig. 4.6 LAS fitted curves for γ-irradiated $Ni_{0.5}Cu_{0.2}Cd_{0.3}Fe_{2-x}Al_xO_4$ nanoparticles.

The fitted curves are shown in solid lines and very well-fitted lines are observed through this process. The fitted parameters are listed in Table 4.2.

Table 4.2 LAS fitted parameters

Irradiation dose	1 MRad					3 MRad				
Al content	0	0.015	0.03	0.045	0.06	0	0.015	0.03	0.045	0.06
M_s, emu/gm	54.78	60.31	70.12	59.04	42.18	57.26	65.54	85.59	74.14	48.91
M_s, (LAS) emu/gm	54.99	61.90	69.49	59.91	43.06	57.15	65.55	85.26	73.53	48.95
K	3708.07	3817.19	2156.89	4214.09	3584.37	3431.14	3067.07	2797.88	2476.31	3386.74

4.3 DIELECTRIC STUDY

The dielectric constant is termed as how much material is capable to storing electric energy. The change in behavior of complex dielectric constant (ε*) with irradiation at room temperature shows the dynamics of various polarization. A sharp decrease has been observed in the dielectric constant curve against the increasing frequency.

The dielectric study is essential for ferrite which is dependent on the composition of the compound, condition of synthesis, presence of cations, and course the temperature of synthesis. Fig. 4.7 shows the variation of the real component of the dielectric constant ($\varepsilon^{/}$) against the frequency at room temperature for $Ni_{0.5}Cu_{0.2}Cd_{0.3}Fe_{2-x}Al_xO_4$.nanoparticles for both 1MRad and 3MRad irradiated samples. The investigation has been taken within the frequency range of 20 Hz and 15 MHz.

This range is the same for both types of samples (after irradiation) dispersion behavior of $\varepsilon^{/}$ is observed in the lower frequency regime (*20Hz-1kHz*) whereas it slowly in the frequency

domain (*1kHz-1MHz*) and turns frequency-dependent afterward. $\varepsilon^{/}$ tends to decrease in the lower range of frequency and at the higher frequency range, the variation is the same as at both irradiation. $E^{/}$ display lower values i.e. the nanoparticles exhibit lower dielectric which has a very important view for the application. Similar behavior was also observed by other researchers [63-69].

4.3.1 Frequency Dependence of Real Part of Dielectric Constant

The rapid decrease is evident at initial frequencies whereas an almost frequency independent nature is evident in higher frequencies. Such type of nature is known as normal behavior of dielectrics [70-71]. Depending on the dielectric polarization content the above behavior can understood. Space charge polarization can explain that nature too. So, the conduction system of ferrites governs the nature of $\varepsilon^{/}$ [72], where hopping between electrons takes place. Low field application of frequency favors the electron hopping mechanism. Therefore, $\varepsilon^{/}$ is large at low frequency.

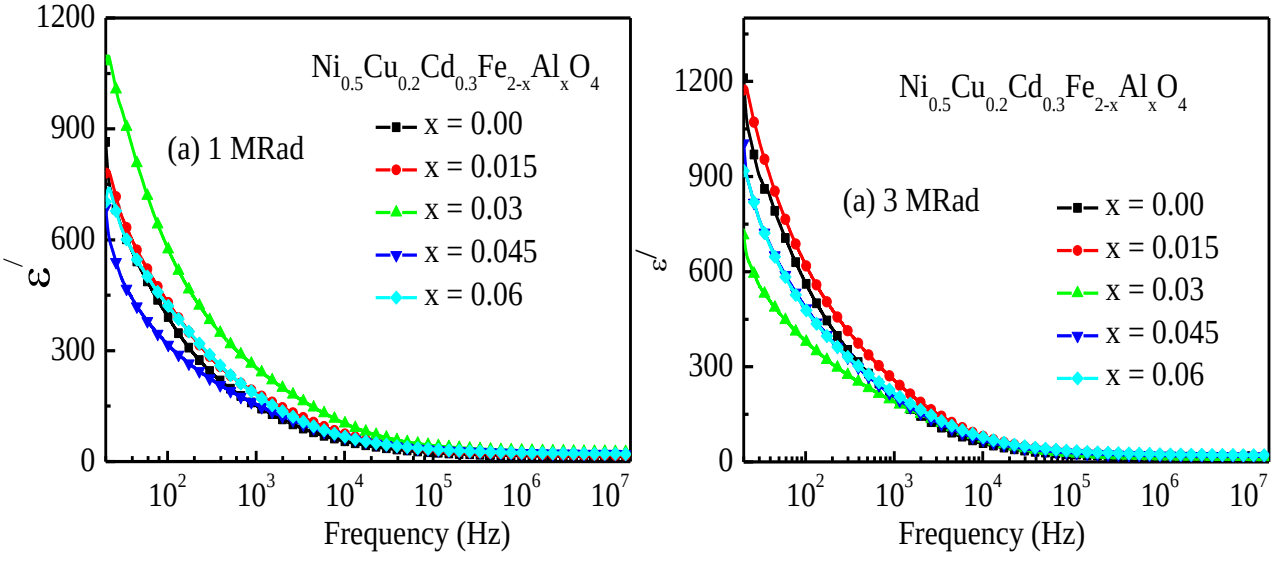

Fig. 4.7 Variation of real part of dielectric constant as a function of frequency for (a) 1 MRad and (b) 3 MRad γ irradiation of $Ni_{0.5}Cu_{0.2}Cd_{0.3}Fe_{2-x}Al_xO_4$.

The exchange of electrons between Fe^{3+} and Fe^{2+} generates local displacement of the electron along the applied electric field. As a result, polarization is induced in ferrites. The exchange of electrons follows the applied alternating field only when the frequency is less than a certain value. Hence the dielectric constant becomes steady with a smaller value [73-77]. In addition, a slight increase for $\varepsilon^{/}$ is observed in Fig. 4.6. with γ irradiation. The interaction between gamma irradiation and ferric ions is as follows,

$$Fe^{2+} + \gamma \rightarrow Fe^{3+} + e^{-}$$

The creation of B site preference of ferrous ions has resulted from the interaction and thus ratio of Fe^{2+}/Fe^{3+} increases on these sites [78-82]. The orientation of hopping electrons rises the magnitude of $\varepsilon^{/}$ along the direction of the field.

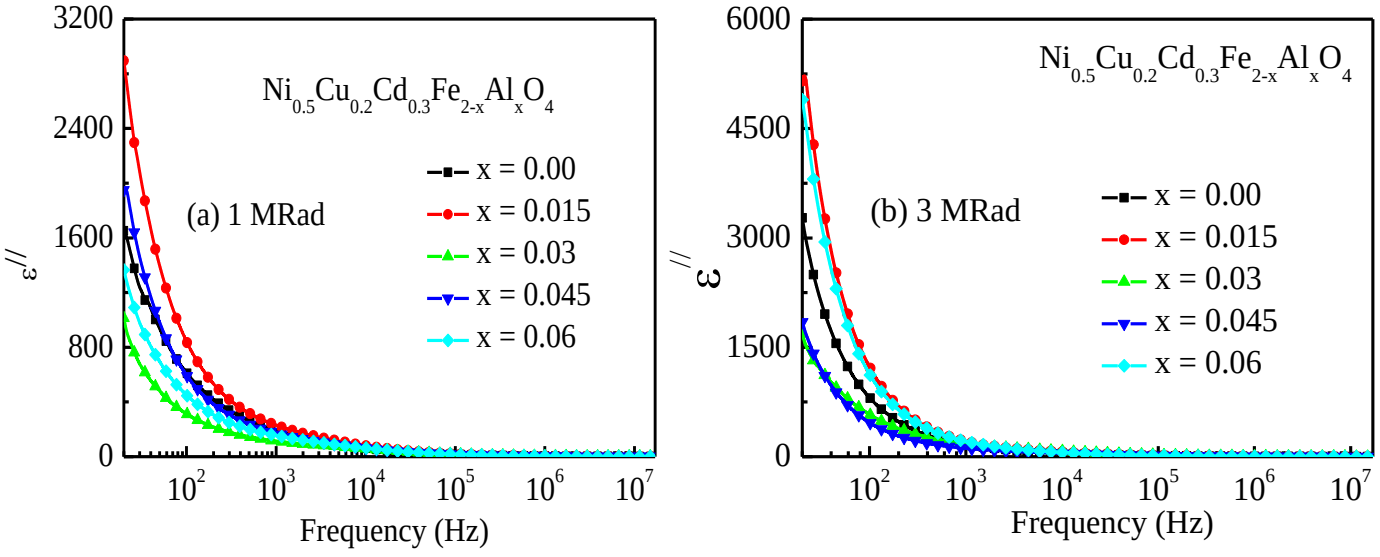

Fig. 4.8 Variation of imaginary part of dielectric constant as a function of frequency for (a) 1 MRad and (b) 3 MRad γ irradiation of $Ni_{0.5}Cu_{0.2}Cd_{0.3}Fe_{2-x}Al_xO_4$.

4.3.2 Frequency Dependence of Imaginary Part of Dielectric Constant

The imaginary component of the dielectric constant (ε") or the dielectric loss versus frequency plot for the investigated samples, (with γ irradiation with different doses) at room temperature is illustrated in Fig. 4.7. The continuous decrease of ε" till a certain frequency, is observed for an increase in frequency and remains constant afterward. The irradiation processes of γ increase the values of ε" of every sample. A similar decline in the value of ε" against increasing frequency has been reported for other ferrites research [83-86]. The increment in the value of γ irradiated ε" was also reported in [87]. Such types of declining ε" are explained as follows. The main loss of ferrites consists of many factors: eddy current loss and dipole loss in addition to the loss of hysteresis.

It is known that resistivity and eddy current are inversely related to each other. At all frequencies, the sample's resistivities decrease. From Fig. 4.6 and Fig. 4.7 (discussed later) high dielectric losses is observed and in Fig 4.15 low value resistances for both grain and grain boundary. For unirradiated case [88] dielectric losses are lower as well as resistivity is higher which support resistivity and eddy current are inversely related. It occurred because the orientation of the dipole does not follow the frequency of the applied field. Furthermore, there is a proportional relationship between the hysteresis loss and the frequency [89]. This means that the effect of both the eddy current and the hysteresis losses is to increase the core loss while the dipole loss decreases the core loss. The competition between the different types of losses determines the behavior of ε" and seems to be responsible for the constancy of losses at high frequencies. Some ferrites showed peaking behavior in the plot of ε" [90]. The peaking condition at the (ε" vs. f and *tanδ* vs. f in Fig. 4.7 for non-Debye relaxation i.e. Havriliak–Negami relaxation) is followed by the same expression [91].

$$\omega\tau = 1$$

where $\omega = 2\pi f_{max}$ is the angular frequency and τ is representing the relaxation time which is related to probable jumping for each unit time, P, by the equation $\tau = {}^{1}/_{2}P$ i.e. $f_{max} \propto P$ [92]. This relation shows that f_{max} is directly proportional to the probability of hopping. The disappearance of f_{max} by the samples implies a low hopping probability, which may be due to the high resistivity. This outcome is in agreement with the previous report for Li-Mg-Ti ferrites where a maximum loss was observed only for low resistive composition [93]. Moreover, the low probability of hopping means that the relaxation times for the investigated samples seem to be large at room temperature ε" but decreases with frequency. The increase in irradiated ε" by γ and neutron irradiations could be due to resistivities decreased by the irradiation process and the effect of resistivity is to increase the loss of eddy current and ε" is increased consequently by providing good agreement with the expression [94]:

$$\rho_{AC} = \frac{1}{\varepsilon/\varepsilon_0 \omega}$$

4.3.3 Frequency Dependence of Dielectric Loss Tangent

The *tanδ* changes can be originated in ferrites because of two mechanisms: (1) hopping of electrons and (2) defects in charged dipoles. The initial decline of *tanδ* with increasing frequency is extracted by the principle of Koop's phenomenological theory of dielectrics [95]. In the lower frequency region, the higher loss factors in both cases are observed due to the phase delay of hopping charge with a frequency that possesses high resistivity for grain boundaries and requires more energy to exchange electrons among Fe^{3+} and Fe^{2+}.

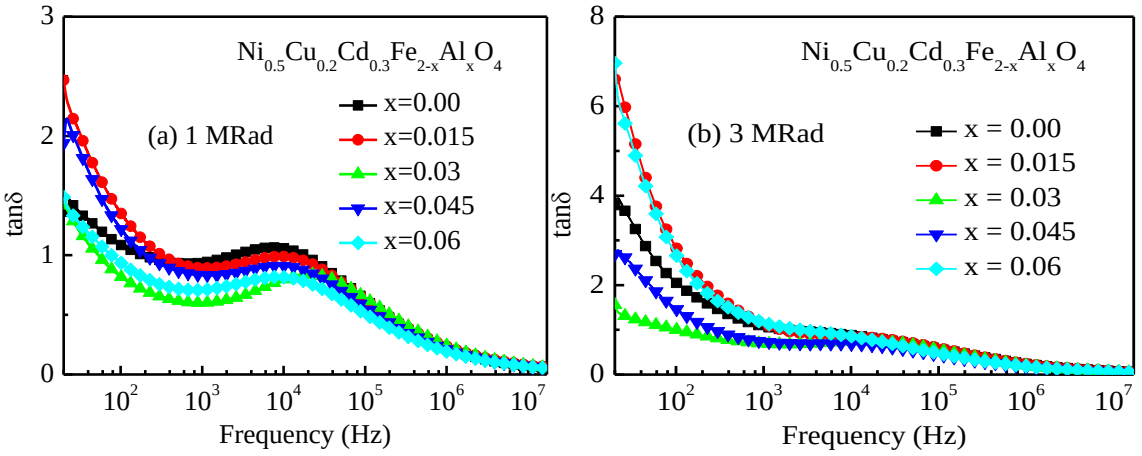

Fig. 4.9 Variation of tanδ as a function of frequency for (a) 1 MRad and (b) 3 MRad γ irradiation of $Ni_{0.5}Cu_{0.2}Cd_{0.3}Fe_{2-x}Al_xO_4$.

Thus a high loss in energy is observed. On the other hand, less loss in energy is observed for low resistive grain at a higher range of frequency (15 MHz). Also, the peak height decreases as a dose of irradiation increases. Rezlescu Model can explain the loss tangents peaking behaviour [96].

The position of the peak transmits toward low frequency for the increasing dose of irradiation. This depicts the decrease in the probability of jumping with the increasing content of Al. Hence, Fe^{3+} occupancy on B-sites has decreased and caused polarization on ferrites ions. As Fe^{3+} on the B-site decreases, the height of the peak tends to go down. The board peak appears at which superimposition between hopping frequency and external field frequency takes place, the transformation from the highest electrical energy to the oscillatory ions has occurred and consequently, a peak for highest power loss is observed. This peak is related to the dielectric relaxations phenomenon, provided the condition $\omega\tau = 1$ is satisfied and also for the resonance of domain wall (i.e. contribution of grain-grain boundary) [97] and a similar type of dielectric constant behaviour has also been reported by Batoo et al. [63], Ramay et al. [64], Ramesh et al. [65], Hashim et al. [66]. At both annealing temperatures, the observed low dielectric values by the investigated ferrites make them ideal for high-frequency application points of view.

Therefore, the relatively low loss makes prepared samples applicable at higher frequencies in technical sectors and it is also compatible with another result found by Batoo et al. [63] having a loss factor at 5 kHz.

4.4 ELECTRIC MODULUS SPECTROSCOPY

A complex modulus study is a vital tool that is useful to interpret the dynamic aspect of the transport process of electrical behavior inside the material. Several parameters occur including the hopping rate of carrier or ion, the smallest capacitance at high frequencies containing relaxation time of conductor in the system of dielectric and thereby large dielectric constant magnitude at low-frequency range is minimized.

Modulus spectrum analysis has grown interested gradually in both types of conduction analysis (ionic and electronic) in the materials. Through this study, it is possible to characterize the insight of the electrical process even for materials' tiny capacitance. Modulus spectroscopy can suppress electrode polarization effects [98] and also unwanted relaxation effects of extrinsic nature. The relation between electric modulus and the complex permittivity is given as follows [99]:

$$M^* = (\varepsilon^*)^{-1} = \frac{\varepsilon'}{\varepsilon'^2+\varepsilon''^2} + i\frac{\varepsilon''}{\varepsilon'^2+\varepsilon''^2} = M' + iM''$$

$$M_\infty = \left[1 - \int_0^\infty e^{-i\omega t}\left\{\frac{d\varphi}{dt}\right\}\right]$$

where M′ represents the real part of the electric modulus and M′′ represents the imaginary part of the same quantity. Moreover, $M_\infty = 1/\varepsilon_\infty$ has an inverse character with the dielectric permittivity of high frequency. The relation between the time evolution function φ(t) and the decay function of relaxation time in the dielectric is expressed as follows [100]:

$$\varphi(t) = \exp\left[-\left(\frac{t}{\tau_{M''}}\right)^{\beta}\right] \; 0<\beta<1$$

Where $\tau_{M''}$ and β are the most probable relaxation time and the stretched exponent parameter respectively. Debye and non-Debye relaxation can be indicated from the values of $\tau_{M''}$ and β. From the perspective of physical point, the constant electric displacement has been found during correspondence of relaxation time of electric modulus in the electric field. A broad asymmetric peak and a sigmoidal behavior are the general features of the imaginary and real part of the electric modulus [101-103].

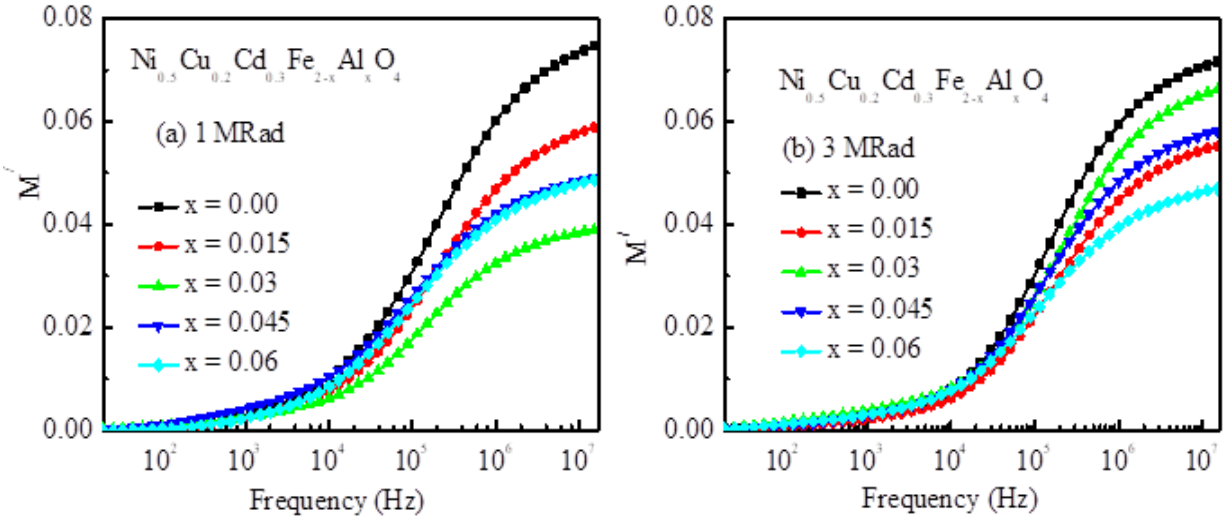

Fig. 4.10 Variation of real part of electric modulus as a function of frequency for (a) 1 MRad and (b) 3 MRad γ irradiation of $Ni_{0.5}Cu_{0.2}Cd_{0.3}Fe_{2-x}Al_xO_4$.

The real electric modulus is very low at lower frequencies and after a certain range of frequency, it creases gradually and reaches saturation. Due to the scarcity of restoring force, M′ becomes saturated with the possibility at high frequency [104].

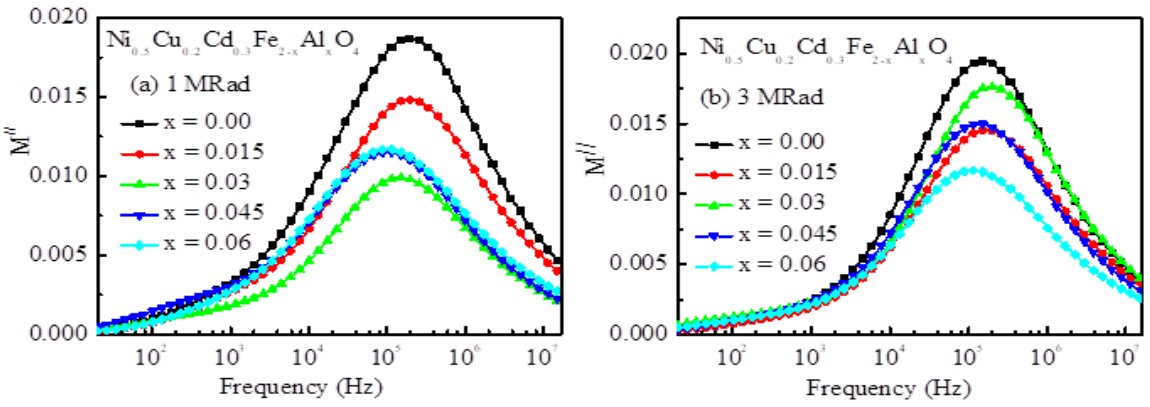

Fig. 4.11 Variation of imaginary part of electric modulus as a function of frequency for (a) 1 MRad and (b) 3 MRad γ irradiation of $Ni_{0.5}Cu_{0.2}Cd_{0.3}Fe_{2-x}Al_xO_4$.

This behaviour appears at a lower domain frequency to give smaller M´ leading to the process of conduction for the long-range motion of charge carriers and polarization of electrode contributes negligibly to the material [105].

The M´ and M´´ dependence on frequency for both irradiation by gamma of Ni-Cu-Cd-Al ferrite samples are illustrated in Fig. 4.10 and Fig. 4.11 respectively. It is depicted from Fig. 4.10 for irradiation by a different dose that M´ increase slightly at the beginning within the region of low frequency and increase remarkably in the region of high frequency. Whereas, M´´ depicts (in Fig. 4.11) peaking behaviour.

M´´ max is thought to be the highest value that occurs at characteristic frequency. The characteristic frequency is also assigned as the relaxation frequency (indicated by $f_m^{//}$) which is applicable for relaxation time ($\tau_M^{''}$) evolution. The $M^{//}$ illustrates the dissipation of energy that occurred in the process of irreversible conduction indicating the highest loss of conduction at the center of $M^{//}_{max}$ [106].

The modulus Cole-Cole plots for all samples are illustrated in Fig. 4.12. The irradiated samples reveal single semicircular shapes with a center below the real axes. Thus these illustrations depict grain conduction and grain boundary conduction is not seen here.

The various diameters of various semicircles predict the grain values that are equivalent to electrical parameters. The value of β represents the tilt angle for the circular arc which lies between 0 and 1. In this way, it explains the Debye nature and non-Debye nature of relaxation inside the materials. The lower than 1 value of β is an indication of non-Debye relaxation of dipole-dipole interaction for the investigated samples. Previous results confirm the dominance of properties through the semicircular curve [107, 108].

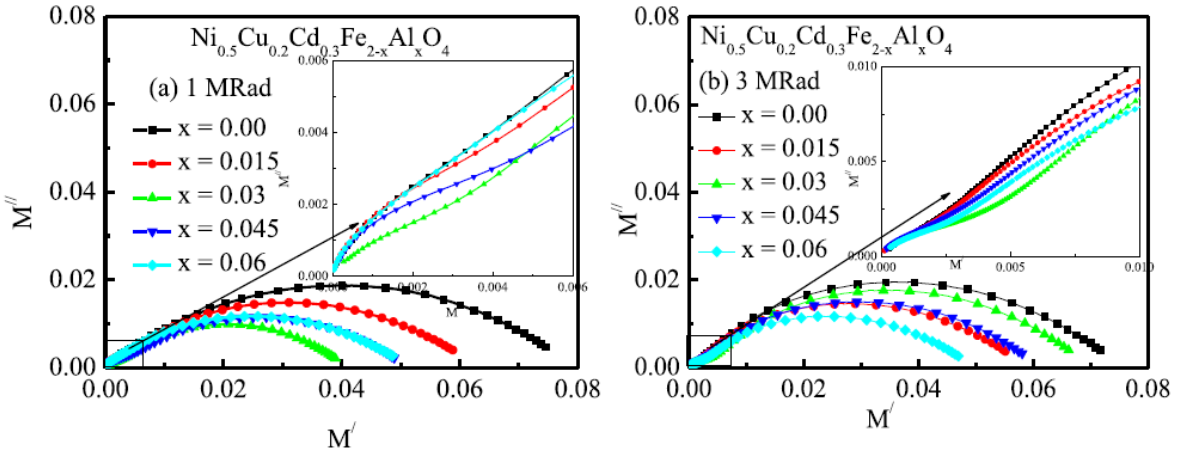

Fig. 4.12 $M^{/}$ vs $M^{//}$ plot of $Ni_{0.5}Cu_{0.2}Cd_{0.3}Fe_{2-x}Al_xO_4$ for (a) 1 MRad and (b) 3 MRad γ-irradiation.

The complex modulus study also gives the idea of electric stiffness through the semicircle. The Cole-Cole plots in Fig. 10(a) and Fig. 10(b) reveal the dominated property of electrical stiffness of studied materials.

4.5 IMPEDANCE ANALYSIS

Impedance spectroscopy explains the correlation between microstructure and dielectric properties. Besides, it unravels materials complexity which controls the properties of the

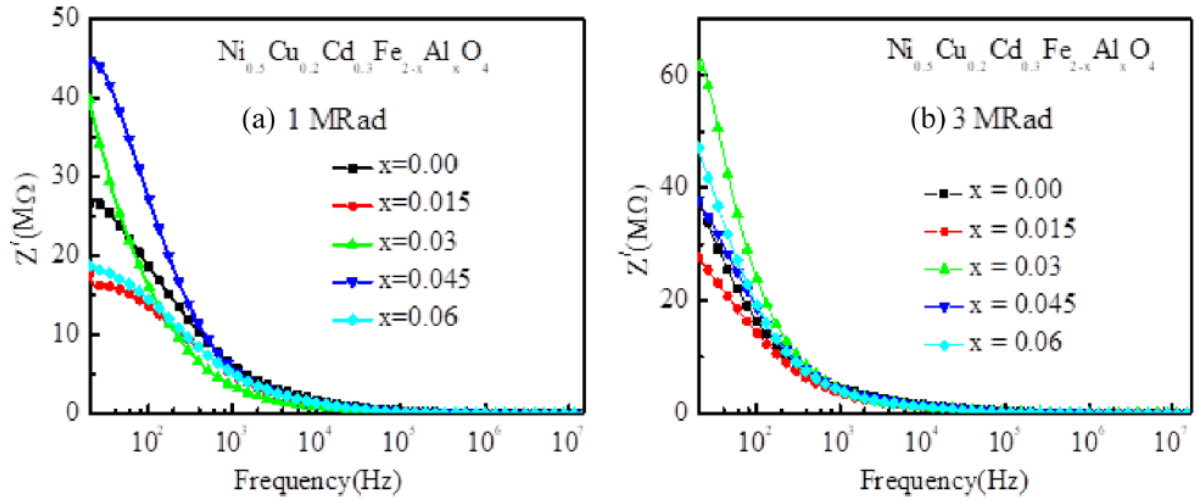

Fig. 4.13 Variation of real part of impedance as a function of frequency for (a) 1 MRad and (b) 3 MRad c irradiation of $Ni_{0.5}Cu_{0.2}Cd_{0.3}Fe_{2-x}Al_xO_4$.

structure, ceramic texture, composition, distribution of defects, and dopants themselves, and their applications also depend on that. Impedance analysis is effective as the grain impedance is separated by grains boundary impedance and electrode impedance effects.

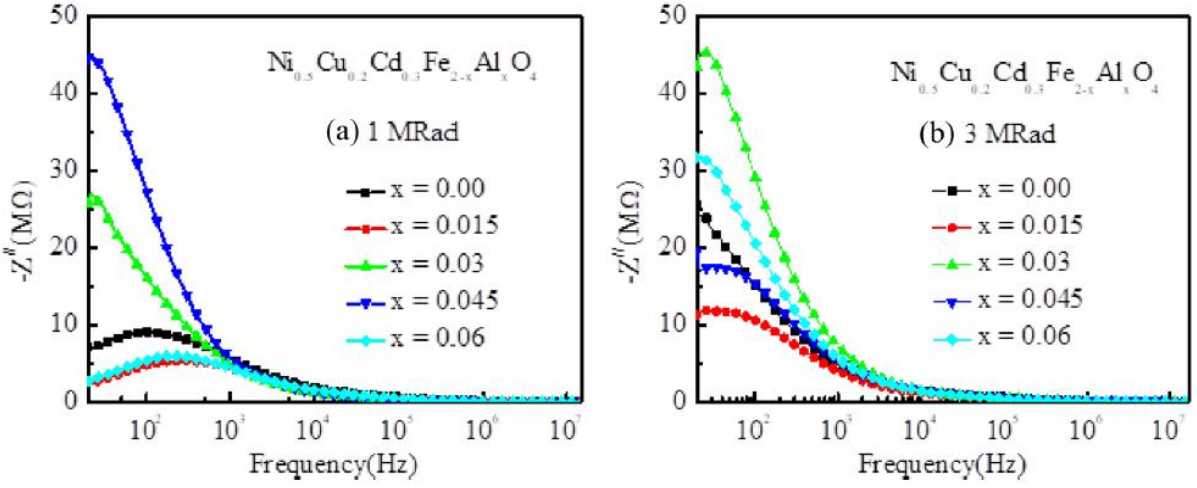

Fig. 4.14 Variation of imaginary part of impedance as a function of frequency for (a) 1 MRad and (b) 3 MRad c irradiation of $Ni_{0.5}Cu_{0.2}Cd_{0.3}Fe_{2-x}Al_xO_4$.

It is observed through the frequency-dependent nature of the constituent [109]. Based on a specifically efficient circuit model which consists of electrical discrete equipment. The process involves the accomplishment of observed data to form a circuit equivalent to the data for investigating materials [110]. Resistive and reactive portions for corresponding materials are included in the measurements of impedance data. Fig. 4.13 (a) and Fig. 4.13(b) and Fig. 4.14 (a) and Fig. 4.14 (b) represent both the real and imaginary parts of impedance after gamma irradiation.

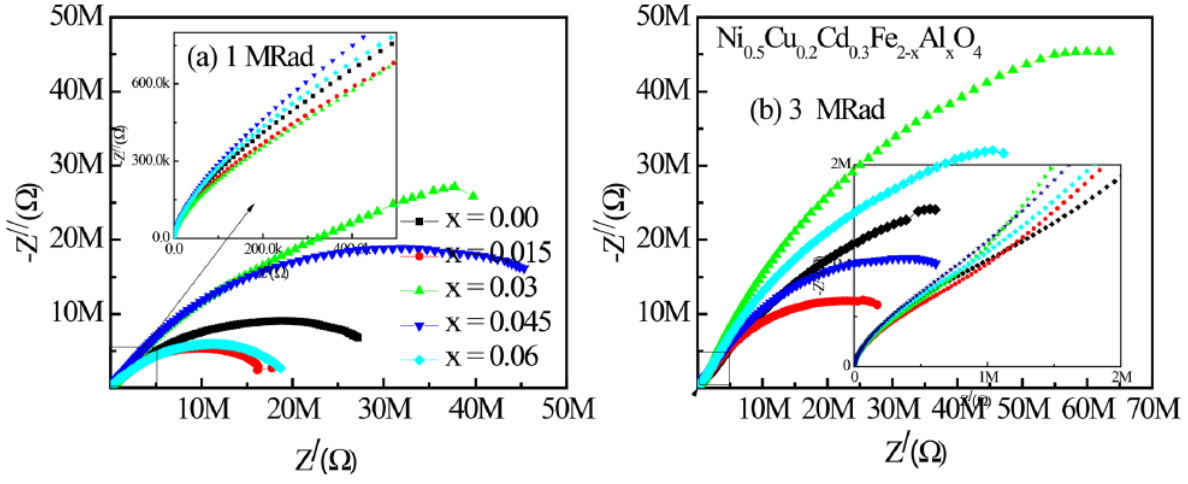

Fig. 4.15 $Z^{/}$ vs $Z^{//}$ Cole–Cole plots of $Ni_{0.5}Cu_{0.2}Cd_{0.3}Fe_{2-x}Al_xO_4$ for (a) 1 MRad and (b) 3 MRad γ irradiation.

In the diagrams of complex impedance, the imaginary part variation with the real part of the impedance is plotted.

Table. 4.3 Cole-Cole fitted data

Irradiation dose	1 MRad					3 MRad				
Al content	0.00	0.015	0.03	0.045	0.06	0.00	0.015	0.03	0.045	0.06
R, MΩ	21.03	12.85	34.36	37.78	14.23	2.46	20.79	64.12	29.85	40.16
C_g, μF	48.86	49.81	32.88	35.12	47.77	0.29	0.42	0.28	0.4	0.33
R_g, MΩ	0.72	0.71	0.61	0.42	0.1	0.34	0.53	0.59	0.6	0.72
τ_g, μs	2.03	1.87	2.4	2.46	2	0.51	2.16	2.71	2.23	2.34
α_g	0.43	0.39	0.34	0.37	0.43	0.15	0.42	0.32	0.46	0.36
C_{gb}, μF	1	1.06	1.02	1.05	1.03	0.06	1.02	1.02	1.05	1.03
R_{gb}, MΩ	0.13	0.6	0.89	0.91	0.96	25.67	0.89	0.89	0.8	0.1
τ_{gb}, μs	0.04	0.04	0.02	0.02	0.04	0.0003	0.35	0.22	0.31	0.25
α_{gb}	0.39	0.39	0.27	0.27	0.39	0.61	0.34	0.23	0.33	0.27

This representation (Fig. 4.15 (a, b)) is expected for the distinct relaxation of the material if magnitudes are comparable and satisfy the functional forms of Cole-Cole. The probable outcome is a pair of semicircles regarding electrical properties. Among the two semicircles, the former is generated for grain boundary in a lower region of frequency, and the latter is generated for the grain resistance in a higher range of frequency [111]. The electrodes interface's contribution can generate a smaller arc in the case of enough frequency in a lower region [112].

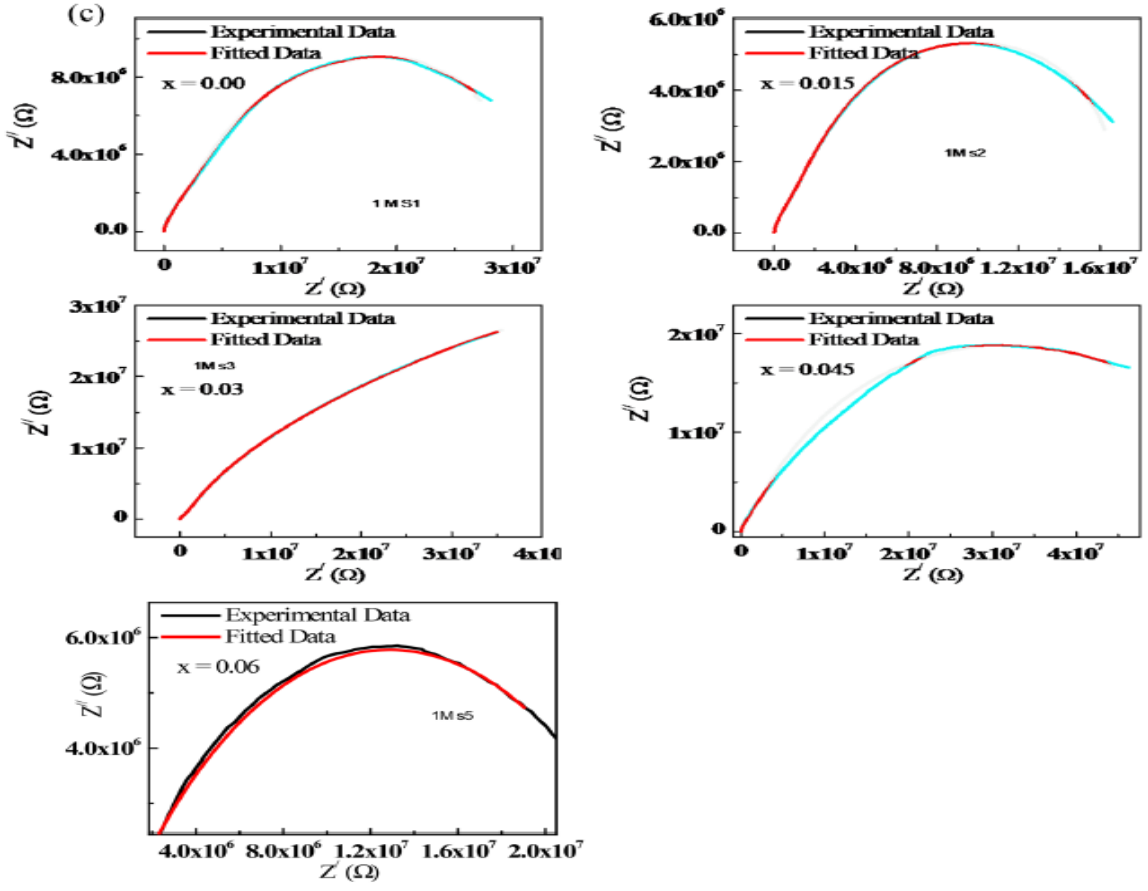

Fig. 4.15 (c) Cole–Cole Fitted plots for 1 MRad radiated samples

The theoretical Cole-Cole fitted plots for impedance data are shown in Fig. 4.15 (c) (for 1M samples) and Fig. 4.15 (d) (for 3M samples). From the two superimposed semicircles,

the former one corresponds to grain whereas the latter one is for grains boundaries at higher and lower frequencies respectively.

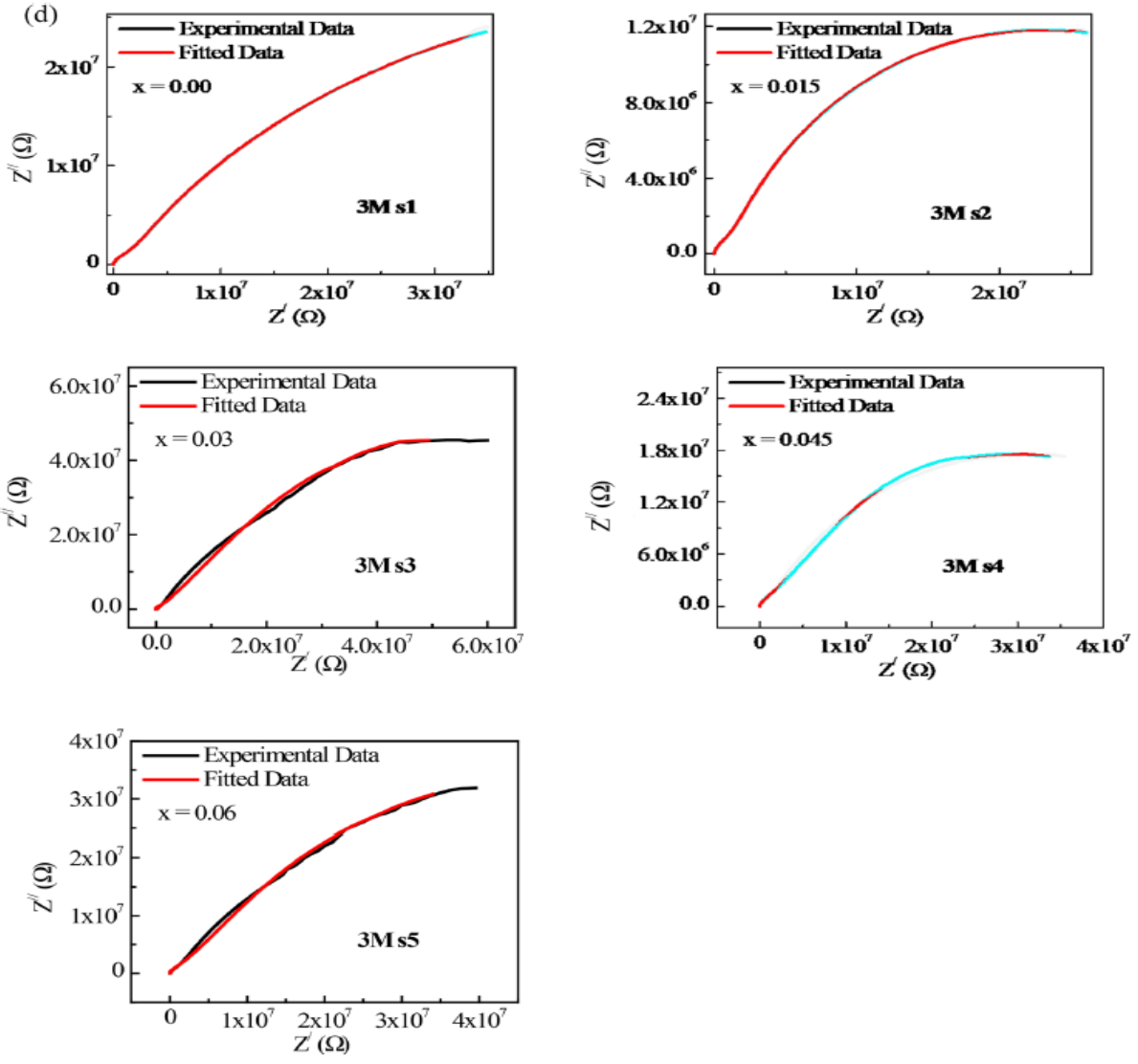

Fig. 4.15 (d) Cole–Cole Fitted plots for 3 MRad radiated samples

They exhibit the wider semicircles overlap for nano particles which is similar to the report of Philippe Knauth et al. [85]. The fitted parameters are listed in Table 4.3. The values of R_g show a decrease with the substitution of Al for gamma irradiation dose whereas

the values of R_{gb} show an increase with the substitution. This agrees well with the ac conduction result interpretation for all samples.

4.6 AC CONDUCTIVITY STUDY

The ac conductivity has been measured at room temperature. The frequency dispersion is exhibited at room temperature by the ac conductivity between the range of frequency 3×10^2 Hz and 5×10^5 Hz. Ac conductivity changes for samples with irradiation are determined in various fluences. Fig. 4.16 shows the variation in conductivity (σ_{ac}) of all prepared $Ni_{0.5}Cu_{0.2}Cd_{0.3}Fe_{2-x}Al_xO_4$ ferrite nanoparticles at room temperature and with gamma irradiation at different doses. The σ_{ac} increases comparatively slowly with frequency up to 10^3 kHz and thereafter it rises rapidly at both irradiation and different doses.

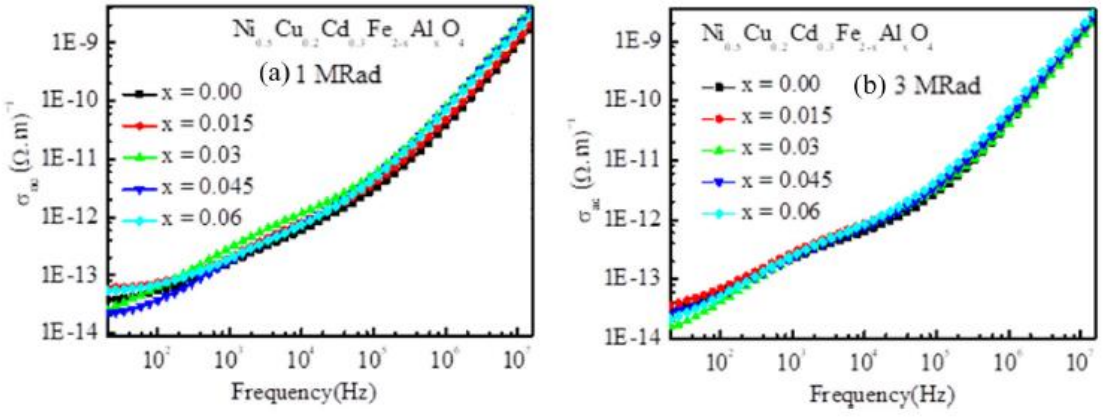

Fig. 4.16 Variation in ac conductivity of $Ni_{0.5}Cu_{0.2}Cd_{0.3}Fe_{2-x}Al_xO_4$ nanoparticles with (a) 1 M γ irradiation and (b) 3 M γ irradiation.

The main reason for the electrical conductivity is the electrons hopping among elemental ions of the same type which possess diverse valences throughout the lattice sites of the crystal. The distance of metal ions on A sites (0.357 nm) is greater than that of the B sites (0.292 nm) in the

close-packed cubic system of oxygen. For this reason, A⇔ B sites hopping of electron is less probable than the B⇔B sites. Due to the largest distances among Cd^{2+} and Fe^{3+}, the hopping is less probable in A⇔A sites. Hence Fe^{2+} prefers to be occupied by the B sites only as they are formed in the sintering mode [106]. Koop's phenomenological model is applicable for explaining the variety nature of σ_{ac} as a function of frequency [107]. This model implies that, grain boundary conduction leads σ_{ac} at a lower range of frequency while grain conduction leads to it at higher frequencies [108].

Alder and Feinleib [109] reported the linear increase in ac conductivity against frequency during small polarons' conduction. The conduction mechanism occurs predominantly for the contribution of grains in a higher range of frequencies. Austin-Motto [101] explained a model for the polaron hopping which describes the dependence of conductivity with frequency. The model shows the upward trend of σ_{ac} against frequency increment for polaron hopping in the small range and a downward trend in polaron hopping in the long range. The conductivity is not dependent on frequency when band conduction is considered [59]. The total electrical conductivity is given by the following relationship for ferrite materials

$$\sigma(f, T) = \sigma_{dc}(T) + \sigma_{ac}(f, T) \quad (8)$$

where σ_{dc} depends on temperature only due to band conduction and is termed as dc conductivity. The next term σ_{ac} depends on both frequency and temperature which is termed pure ac conductivity and imposed B site hopping mechanism. The following empirical formula expresses the σ_{ac} dependency on frequency [18]:

$$\sigma_{ac}(f) = Af^n \quad (9)$$

where, A and n are constants in which n has no dimension where A has units same as σ_{ac}. Both of them are dependent on composition and temperature.

CHAPTER 5: CONCLUSIONS

5.1 GENERAL

In this study, the effect of gamma (γ) irradiations on the structural, magnetic and electrical properties of nanoferrites with the chemical formula $Ni_{0.5}Cu_{0.2}Cd_{0.3}Fe_{2-x}Al_xO_4$ *have studied.*

5.2 KEY FINDINGS

According to the obtained results, the following key findings could be mentioned.

- After γ irradiation, the spinel single phase structure remain unaltered have observed.
- The samples' XRD spectra following γ irradiation revealed shifts in the peaks' relative intensities as well as changes in peak shifts. These outcomes has attributed to the deformation brought about by irradiation in the cubic lattice.
- Gamma irradiation of $Ni_{0.5}Cu_{0.2}Cd_{0.3}Fe_{2-x}Al_xO_4$ nano ferrite decreases its particle size (L), while it increases the unit cell volume, and room temperature values of M_s, $\varepsilon^{/}$, tanδ and σ.
- The crystallite size shrink following the γ irradiation procedures. Furthermore, a possible explanation for the little rise in the lattice constant across all samples under investigation is the transformation of some Fe^{+} ions (0.67Å) into Fe^{2+} ions (0.76 Å).
- From the M-H curve, it is clear that at room temperature the nanocrystalline samples of $Ni_{0.5}Cu_{0.2}Cd_{0.3}Fe_{2-x}Al_xO_4$ are in ferrimagnetic state. The saturation magnetization (M_s) increase with increasing gamma irradiation dose. This result could be explained on the basis of cation distribution and exchange interaction between A and B sites. The presence of random canting of nanoparticles brought on by anti-ferromagnetic exchange interactions as a result of gamma irradiation at varying doses is responsible for the increase of M_s.
- For every composition, it is observed that the dispersion curves for the dielectric constant (έ), dielectric loss (ε"), and ρ_{AC} decreased with frequency. After being exposed to γ and

neutron radiation, the levels of ε' and ε" likewise fell. The two layers concept, often known as Kopps' model, was used to explain these findings.

- The samples' corresponding incomplete semicircles are depicted in two overlapping plots of Z' vs. Z''. The first occurs at low frequencies and is caused by the resistance of the grain boundaries, where it is difficult to determine their electrical parameters. The second occurs at high frequencies and is caused by the conduction of the grains, which have higher capacitance and lower resistance than the grain boundaries and exhibit a significant change in their values in response to the dose of γ-irradiation.
- The dynamics of conduction of the studied materials is the predominant property after the irradiation dosage, as shown by the semicircular arc (M'' vs. $M^{/}$) as well as remains non-Debye nature.

Limitation of the Study

The available raw materials used directly without further justification. Due to lack of proper availabilty of machinary during research time Temperature dependent magnetization and Magnetocaloric effect could not be done.

Practical Implication

The result found potential for high radiation environment like nuclear reaction facilities and high energy acceleration etc.

Recommendation for Further Study

Mössbauer effect analysis, Temperature dependent magnetization, Magnetocaloric effect, PE loop, and isotope changes after irradiation can be analyzed.

BIBLIOGRAPHY

[1] J. Smit, Magnetic Properties of Materials, second ed. Mc-Grew Hill, New York, 1972.

[2] A. Yang, C. N. Chinnasamy, J. M. Greneche, Y. Chen, S. D. Yoon, K. Hsu, C. Vittoria, V. G.Harris, Appl. Phys. Lett. 94 113109 (2009).

[3] Y. Ahn, E. J. Choi, S. Kim, D.H. An, K. U. Kang, B. G. Lee, K. S. Baek, H. N. Oak, J. Korean Phys. Soc. 41 123 (2002).

[4] M. K. Roy, B. Halder, H. C. Verma, Nanotechnology 17 232 (2006).

[5] H. Xue, Z. Li, X. Wang, X. Fu, Mater. Lett. 61 347 (2007).

[6] J. P. Singh, R. C. Srivastava, H. M. Agrawal, R. P. S. Kushwaha, P. Chand, R. Kumar, Int. J. Nanosci. 7 21 (2008).

[7] S. T. Assar, H. F. Abosheiasha, A. R. El Sayed, Journal of Magnetism and Magnetic Materials 421 355 (2017).

[8] M. A. Ahmed, S.I. El-dek, S. F. Mansour, N. Okasha, Solid State Sciences 13 1180 (2011).

[9] Yu G. Chukalkin, B. N. Goshchitskii, S. F. Dubinin, S. K. Sidorov, V. V. Petrov, V. D. Parkhomenko, V. G. Vologin, Phys. Stat. Sol. (a) 28 345 (1975).

[10] V. V. Petrov, Yu G. Chukalkin, B. N. Goshchitskii, Sov. Phys. Solid State 22 339 (1980).

[11] M. A. Mousa, M. A. Ahmed, Journal of Material Science 23 3083 (1988).

[12] M. A. Mousa, A. M. Summan, M. A. Ahmed and A. M. Badawy, J. Mater. Sci. 24 2478 (1989).

[13] H. E. Hassan, T. Sharshar, M. M. Hessien, O. M. Hemeda, Nucl. Instrum. Methods Phys. Res. B 304 72 (2013).

[14] L. M. Maheshkumar, S. E. Shirsath, V. N. Dhage, K. M. Jadhav, Nucl. Instrum. Methods Phys. Res. B 269 2026 (2011).

[15] B. Tareev, Physics of Dielectric Materials. Mir, Moscow, 1979.

[16] I. M. Hamada, J. Magn. Magn. Mater. 271 318 (2004).

[17] J. P. Singh, R. Singh, S. Ghosh, A. Tripathi, D. Kabiraj, S. Gupta, T. Som, Ravi Kumar, S. K. Arora, K. Asokan, D. K. Avasthi, D. Kanjilal, N. C. Mishra and G. K. Mehta, Nucl.Inst. Meth. Phys. Res. B 156 206 (1999).

[18] M. Veena, A. Somashekarappa, G. J. Shankaramurthy, H. S. Jayanna, H. M. Somashekarappa, J. Magn. Magn. Mater. 419 475 (2016).

[19] A. Karim, S. E. Shirsath, S. J. Shukla, K. M. Jadhav. B 268 2706 (2010).

[20] K. N. Choo, M. S. Cho, B. H. Jun, C. J. Kim, S. J. Park, 2 837 (2014).

[21] D. Anjana, M. Singh, K. Ravi, Nucl. Instrum. Methods Phys. Res. B 207 296 (2003).

[22] G. Sanjukta, P. Ayyub, N. Kumar, S.A. Khan, D. Banerjee, Nucl. Instrum. Methods Phys. Res. B 212 510 (2003).

[23] M. C. Chhantbar, K. B. Modi, G. J. Baldha, H. H. Joshi, R.V. Upadhyay, K. Ravi, Nucl. Instrum. Methods Phys. Res. B 244 124 (2006).

[24] K. Ravi, S. K. Sharma, D. Anjana, V. V. Kumar, S. N. Dolia, A. Gupta, M. Knobel, M. Singh, Hyperfine Interact. 160 143 (2005).

[25] N. Z. Darwish, O. M. Hemeda, M. I. AbdJElati, Appl. Radiat. Isot. 45 445 (1994).

[26] M. Hemeda, M. ElJSaadawy, J. Magn. Magn. Mater. 256 63 (2003).

[27] D. M. Hemeda, J. Appl. Sci. 2 989 (2005).

[28] E. Ateia, Egypt. J. Solids, 29 317 (2006).

[29] M. A. Ahmed, E. Ateia, G. Abdelatif, F. M. Salem, Mater Chem. Phys. 81 63 (2003).

[30] N.Okasha, J. Alloys Compd., 490 307 (2010).

[31] K. Asif, E. S. Sagar, S. J. Shukla, K. M. Jadhav, Nucl. Instr. and Meth. In Phys. Res. B (2010).

[32] Z. Yue, J. Zhou, L. Li, Z. Wang, Z. Gui, Mater. Sci. Eng., B 86 64 (2001).

[33] A. Vital, A. Angermann, R. Dittmann, T. Graule, J. Töpfer, Acta Mater. 55 1995 (2007).

[34] R. S. Rama, V. Murthy, J. Mater. Sci. 41 (2006) 1475.

[35] B. M. Sahanashreea, E. Melagiriyappaa, H. S. Jayanna, H. M. Somashekarappac, Radiation Physics and Chemistry 139 55 (2017).

[36] M. Veena, G. J. Shankaramurthy, H.S. Jayanna, H.M. Somashekarappa, Journal of Alloys and Compounds 735 2532 (2018).

[37] B. D. Cullity, Elements of X-Ray Diffraction. Addison Wesley, 1978.

[38] J. A. Mydosh, Spin Glasses: an Experimental Introduction, Taylor and Francis, London Washington, DC, 1993.

[39] A. K. Nikumbh, A. V. Nagawade, G. S. Gugale, M. G. Chaskar, P. P. Bakare, J. Mater.Sci. 37 637 (2002).

[40] J.B. Nelson, D.P. Riley. Proc. Phys. Soc. London. 57 160 (1945).

[41] T. L. Templeton, A. S. Arrott, A. E. Curzon, M. A. Gee, X.-Z. Li, Y. Yoshida, P.J. Schurer, J.L. Lacombe. J. Applied Phys. 73 6728 (1993).

[42] Goldman, Handbook of Modern Ferromagnetic Materials, Kulwer Acad. Pub, Boston, USA, 1999.

[43] P.A. Shaikh, R.C. Kambale, A.V. Rao, Y.D. Kolekar.J. Alloys. Compd. 482 276 (2009).

[44] R.C. Kambale, P.A. Shaikh, C.H. Bhosale, K.Y. Rajpure, Y.D. Kolekar.J. Smart Mat. Structr. 18 085014 (2009).

[45] L. Maheshkumar, V. Mane, N. Dhage, P.S. Aghav, M. K. Babrekar, K. M. Jadhav, AIP Conf. Proc. 1349, 1131 (2011).

[46] M.M. Eltabey, I.A. Ali, H.E. Hassan, M.N.H. Comsan, J.Mater. Sci. 46, 2294 (2011).

[47] S. Singhal, S. Jauhar, N. Lakshmi, S. Bansal, J. Mol. Struct. 1038, 45 (2013).

[48] M.A. Mannan, M.B. Hossen, J. Mater. Sci.: Mater. Electron. 32, 24524 (2021).

[49] H.F. Abosheiasha, S.T. Assar, J. Magn. Magn. Mater. 370, 54 (2014).

[50] B. Viswanathan, V.R.K. Murthy, Ferrite materials (Science and Technology, Narosa Publishing House, New Delhi, (1990).

[51] N. Okasha, J. Mater. Sci. 43, 4192 (2008).

[52] O.M. Hemeda, M. El-Saadawy, J. Magn. Magn. Mater. 256,63 (2003).

[53] H.E. Hassan, T. Sharshar, M.M. Hessien, O.M. Hemeda, Nucl. Inst. Methods Phys. Res. B 305, 72 (2013).

[54] G.P. Pells, J. Nucl. Mater. 184, 177 (1991).

[55] R. Dupree, M.H. Levis, M.E. Smith, Philos. Mag. A 53, L17 (1986).

[56] A. Ibarra, R. Vila, M. Jimenez de Castro, Philos. Mag. Lett.64, 45 (1991).

[57] M.F. Mahmood, M.B. Hossen, J. Mater. Sci.: Mater. Electron.32, 14248 (2021).

[58] P.B. Belavi, G.N. Chavan, B.K. Bammannavar, L.R. Naik,R.K. Kotnala, J. Mat. Chem.Phys. 132, 138 (2012).

[60] O.M. Hemeda, Turk. J. Phys. 28, 121 (2004).

[61] D.R. Patil, B.K. Chougule, J. Mat. Chem. Phys. 117, 35 (2009).

[62] S.K. Ahmed, M.F. Mahmood, M. Arifuzzaman, M.B. Hossen, Results in Phsyics. 30, 104833 (2021).

[63] K.M. Batoo, S. Kumar, C.G. Lee, Alimuddin, Curr. Appl.Phys. 9, 826 (2009).

[64] M. Ramay, S.A. Siddiqi, S. Atiq, M.S. Awan, S. Riaz, Chin.J. Chem. Phys. 23, 591 (2010).

[65] T. Ramesh, R.S. Shinde, S.R. Murthy, J. Magn. Magn. Mater. 345, 276 (2013).

[66] M. Hashim, R. Alimuddin, S. Kumar, S. Ali, B.H. Koo, H.Chang, R. Kumar, J. Alloys Compd. 511, 107 (2012).

[67] M.M. Haque, M. Huq, M.A. Hakim, Mater. Chem. Phys. 112, 580 (2008).

[68] M. Chanda, Sci. Eng. Mater. 3, 580 (1980).

[69] D. Ravinder, Mat. Lett. 54, 68 (2004).

[70] N. Rezlescu, E. Rezlescu, Phys. Stat. Sol. 23, 575 (1974).

[71] A.V.R. Reddy, G.R. Mohan, D. Ravinder, B.S. Boyanov, J.Mater. Sci. 34, 3169 (1999).

[72] A.Y. Lipare, P.N. Vasambekar, A.S. Vasambekar, J. Magn.Magn. Mater. 279, 160 (2004).

[73] K.W. Wagner, Ann. Phys. 40, 817 (1913).

[74] V.R.K. Murthy, J. Sobhanadri, Phys. State Solidi. 36, 129 (1976).

[75] R.G. Kharabe, R.S. Devan, C.M. Kanamadi, B.K. Chougule, Smart Mater. Struct. 15, 36 (2006).

[76] M. Ajmal, A. Maqsood, J. Alloys Compd. 460, 54 (2007).

[77] I.M. Hamada, J. Magn. Magn. Mater. 271, 318 (2004).

[78] D.M. Hemeda, J. Appl. Sci. 2, 989 (2005).

[79] E. Ateia, Egypt. J. Solids 29, 317 (2006).

[80] M.A. Ahmed, E. Ateia, F.M. Salem, J. Mater. Sci. 42, 3651 (2007).

[81] M.A. Mousa, A.M. Summan, M.A. Ahmed, Thermochim.Acta 144, 45 (1989).

[82] O.S. Josyulu, J. Sobhanadri, Phys. State Solidi (a) 59, 323 (1980).

[84] S.A. Mazen, Mater. Chem. Phys. 62, 139 (2000).

[85] D. Ravinder, K.V. Kumar, P. Balaya, Mater. Lett. 48, 210 (2001).

[86] E. Otsuki, S. Yamada, T. Otsuki, K. Shoji, T. Sato, J. Appl.Phys. 69, 5942 (1991).

[87] D. Ravinder, A.V. Ramana Reddy, M.G. Ranga, Mater. Lett. 48, 259 (2002).

[88] R.D. Waldron, Phys. Rev. 99, 1727 (1955).

[89] S.S. Bellad, B.K. Chougule, Mater. Chem. Phys. 66, 58 (2000).

[90] C.G. Koops, Phys. Rev. 83, 121 (1951).

[91] N. Rezlescu, E. Rezlescu, Phys. Status Solidi. 23, 575 (1974).

[92] L. Kumar, M. Kar, J. Magn. Magn. Mater. 323, 2042 (2011).

[93] N. Singh, A. Agarwal, S. Sanghi, S. Khasa, J. Magn. Magn.Mater. 324, 2506 (2012).

[94] N. Sivakumar, A. Narayanasamy, N. Ponpandian, G. Govindara,J. Appl. Phys. 101, 1 (2007).

[95] M. Kaiser, Physica B 407, 606 (2012).

[96] A. Mishra, S. N. Choudhary, K. Prasad, R. N. P. Choudhary, Physica B 406, 3279 (2011).

[97] I. Ali, M.U. Islam, M.N. Ashiq, I. Shakir, N.M. Karamat Ishaque, M.N. Akhter, H. M. Khan, M. Irfan, M.A. Khan, Ceram. Int. 41, 8748 (2015).

[98] B.V.R. Chowdari, R. Gopal krishnnan, Solid State Ion. 23, 225 (1987).

[99] S. A. Saafan, A. S. Seoud, R.E. El Shater, Physica B 365, 27 (2005).

[100] S.A. Saafan, Physica B 403, 2049 (2008).

[101] M. Hashim, S. Kumar, S. Ali, B.H. Koo, H. Chung, R. Kumar, J. Alloys Compd. 511, 107 (2012).

[102] M. Abdullah Dar, V. Verma, S.P. Gairola, W.A. Siddiqui, R. K. Singh, R. K. Kotnala, Appl. Surf. Sci. 258, 5342 (2012).

[103] S.A. Mazen, N.I. Abu-Elsaad, Appl. Phys. A 122, 1 (2016).

[104] R.C. Kambale, P.A. Shaikh, C.H. Bhosale, K.Y. Rajpure, Y.D.Kolekar, Smart Mater. Struct. 18, 1 (2009).

[105] P. Knauth, H.L. Tuller, J. Am. Ceram. Soc. 85, 1654 (2002).

[106] S.S. Bellad, B.K. Chougle, Mater. Chem. Phys. 66, 58 (2000).

[107] R.G. Kulkarni, V.U. Patil, J. Mater. Sci. 17, 843 (1982).

[108] M.G. Chourashiya, J.Y. Patil, S.H. Pawar, L.D. Jadhab, Mater. Chem. Phys. 109, 39 (2008).

[109] D. Alder, J. Feinlieb, Phys. Rev. B 2, 31 (1970).

[110] I.G. Austin, N.F. Mott, Adv. Phys. 18, 41 (1969).

[111] A. Vermaa, O.P. Thakur, C. Prakash, T.C. Goel, R.G.Mendiratta, Mater. Sci. Eng. B 116, 1 (2005).

[112] C.A. Hogarth, M.H. Islam, S.S.M.S. Rahman, J. Mater. Sci. 28, 518 (1993).